Thermoelectric Properties of

$Ti_{0.5}Zr_{0.25}Hf_{0.25}Co_xNi_{1-x}Sn$, $Ti_{0.5}Zr_{0.25}Hf_{0.25}NiSn_{1-x}Sb_x$

Half-Heusler Alloys

by

Mathew VanZant

A thesis

presented to the University of Waterloo

in fulfilment of the

thesis requirement for the degree of

Master of Science

in

Chemistry

Waterloo, Ontario, Canada, 2016

Author's Declaration

I hereby declare that I am the sole author of this thesis. This is a true copy of the thesis, including any required final revisions, as accepted by my examiners.

I understand that my thesis may be made electronically available to the public.

Mathew VanZant

Abstract

Energy is essential in today's world as it is used in society on a day to day basis for a variety of applications. However, more than half of the energy produced in the world today is wasted as heat. Due to the climate change and depletion of non-renewable natural resources, both the environment and society would benefit from waste heat recovery. This can be accomplished with thermoelectric materials.

Half Heusler compounds are promising thermoelectric materials due to their large electrical conductivity and Seebeck coefficient values. However, high thermal conductivity has made it difficult to obtain large figures of merit. The highest ZT reported for p-type and n-type Half-Heusler compounds are 0.80 for $Zr_{0.5}Hf_{0.5}CoSb_{0.8}Sn_{0.2}$ and 1.50 for $Ti_{0.5}Zr_{0.25}Hf_{0.25}NiSn_{0.998}Sb_{0.002}$, respectively.

Undoped MNiSn (M = Ti, Zr, Hf) materials were synthesized first in this project. TiNiSn and HfNiSn ternaries displayed ZT values of 0.33 and 0.28 correspondingly. Alloying the M site improved physical properties, as ZT was 0.40 for $Ti_{0.5}Hf_{0.5}NiSn$ and 0.55 for $Ti_{0.5}Zr_{0.25}Hf_{0.25}NiSn$. Doping was optimized next to make further improvements to the figure of merit. Both p-type $Ti_{0.5}Zr_{0.25}Hf_{0.25}Co_xNi_{1-x}Sn$ and n-type $Ti_{0.5}Zr_{0.25}Hf_{0.25}NiSn_{1-x}Sb_x$ materials were synthesized. The highest ZT was 0.18 for $Ti_{0.5}Zr_{0.25}Hf_{0.25}Co_{0.15}Ni_{0.85}Sn$ and 0.82 for $Ti_{0.5}Zr_{0.25}Hf_{0.25}NiSn_{0.99}Sb_{0.01}$. ZrO_2 nano-particles were added to $Ti_{0.5}Zr_{0.25}Hf_{0.25}NiSn_{0.99}Sb_{0.01}$ samples in an attempt to increase ZT through reductions in thermal conductivity. However, power factor losses resulted in no improvement.

Acknowledgements

I would like to thank my professor, Dr. Holger Kleinke for allowing me the opportunity to join his research group as a graduate student so that I may obtain a Masters in Solid State Chemistry. I would also like to thank Holger Kleinke for all of his help and guidance with my research and my thesis writing.

I would also like to thank my previous and current committee members, Dr. Richard Oakley, Dr. Eric Prouzet, and Dr. Pavle Radovanonic for all of their guidance.

I would like to give a special thanks to a few people who I feel made a significant impact during my graduate studies at Waterloo. Thank you Nader Farahi for helping me in the lab, teaching me new laboratory, and helping me improve my knowledge in solid state chemistry. I would like to thank Maegan Rodrigues with her assistance in preparing and running physical property measurements on many of my doped samples. I also appreciate all of Jalil Assoud's help with unit cell refinement on GSAS. I want to thank Parisa Jafarzadeh with all of her help during the writing stage of my thesis.

Finally, I would like to thank all past and current members of the Holger Kleinke research group that have helped me throughout my graduate studies. They include: Katia Kleinke, Nader Farahi, Nhi Truong, Quansheng Guo, Nagaraj Nandihalli, Mohamed Oudah, Rafay Shams, Parisa Jafarzadeh, Yixuan Shi, Cheryl Sturm, Wenbin Ji, and Xiaoyu Cheng.

Table of contents

List of Figures

List of Tables

List of Abbreviations

ZT dimensionless figure of merit

σ electrical conductivity

κ_e electronic contribution to thermal conductivity

HH Half Heusler

HP hot-pressing

κ_l lattice contribution to thermal conductivity

ZT_{max} maximum dimensionless figure of merit

PF power factor

PXRD powder x-ray diffraction

S Seebeck coefficient

SPS spark plasma sintering

κ thermal conductivity

TE thermoelectric

1.0 Introduction

In the world today, energy plays a vital role in society as it is used in many aspects of life on a day to day basis. Energy is essential for driving automobiles, powering factories, refrigerating food, etc… However, over half the energy (~ 60%) produced in the world today is wasted as heat.[1, 33] For example, vehicles using a gasoline-fuelled internal combustion engine are only 25% efficient. When the car is running, gasoline in the gas tank undergoes a combustion reaction, resulting in the production of carbon dioxide and water. Altogether, 40% of the energy from the gasoline is lost from this reaction as it escapes out the exhaust pipe. 30% is transferred to the radiator and is wasted by heating the cooling water. Therefore, only 30% of the energy is transferred to the car and 70% is wasted as heat. However, another 5% is lost due to friction and parasitic losses. Hence, 25% of the energy is used to move and power accessories. This energy pathway is described below in Figure 1.
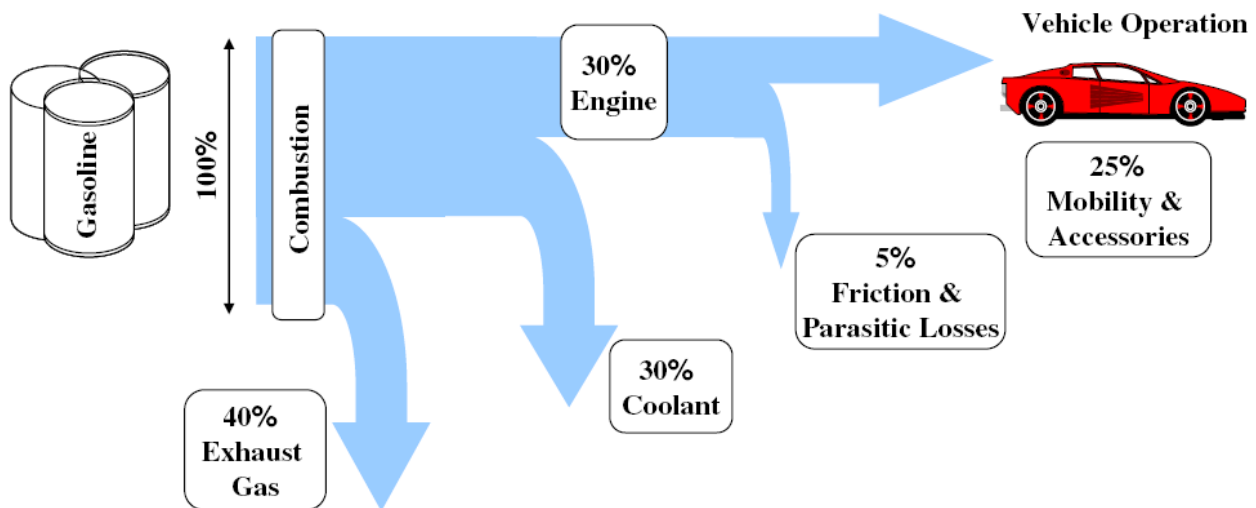
Figure 1: Energy Path for Automobiles with Gasoline Fuelled Internal Combustion Engines[3]

Climate change is currently a global issue as it threatens our way of life. Many studies have shown that the atmospheric concentration of carbon dioxide is increasing, and that it plays a significant role on climate change. Recovering wasted heat and converting it into useful energy would lower CO_2 emissions and therefore benefit the environment significantly.[4] Natural resources such as fossil fuels are a non-renewable resource. Due to their depletion and the large demand for them, recovering waste heat would also be beneficial to society. Recovering waste heat and converting it into useful energy can be accomplished through the use of thermoelectrics.

1.1 Thermoelectric Phenomena

When describing thermoelectrics, there are three fundamental effects to consider. These include the Seebeck effect, the Peltier effect, and the Thomson effect.[37] In 1821, an Estonian-German physicist by the name of Thomas Johann Seebeck discovered the Seebeck effect (Figure 2).[7-9, 12]
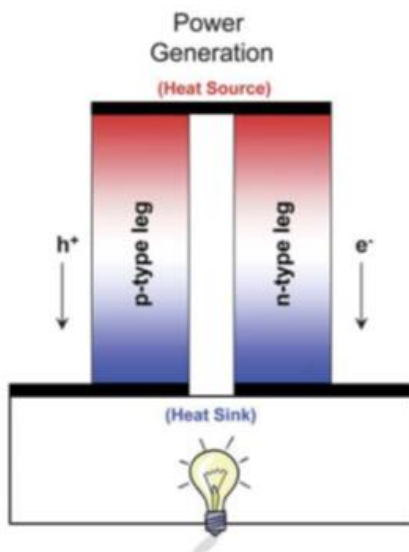
Figure 2: The Seebeck Effect[12]

After creating a temperature difference at the junctions of a closed circuit comprised of two different metals, Thomas Johann Seebeck observed the presence of a magnetic field when his compass needle was deflected. Hence, it was determined that this type of circuit induces an electric current and creates a voltage difference at the two junctions. This phenomenon of generating electrical current by a temperature gradient is today known as "thermoelectricity".[7] Thomas Johann Seebeck also noticed that the voltage difference was proportional to the temperature gradient and depended on the type of conducting material.[10] As shown in Equation (1), the Seebeck coefficient (*S*) relates the voltage difference (Δ*V*) to the temperature gradient (Δ*T*). It is defined as the open circuit voltage that is created between two points on a conductor, when a 1 K temperature difference exists uniformly between the points.[11] An electric current is induced by the movement of charge carriers from the hot side to the cold side.

$$S = \frac{\Delta V}{\Delta T} \qquad (1)$$

In 1834, a French watchmaker and part time physicist by the name of Jean Charles Athanase Peltier discovered the Peltier Effect (Figure 3).[7-9]
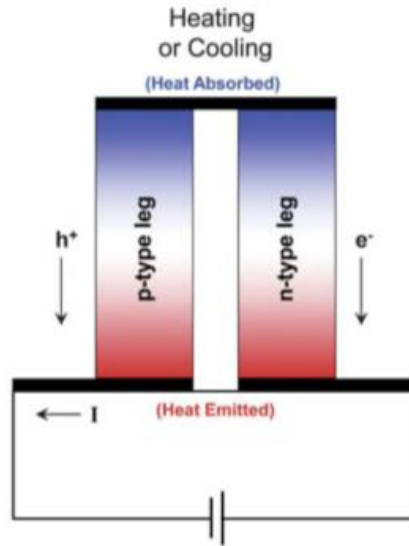
Figure 3: The Peltier Effect[12]

The Peltier effect is simply the reverse of the Seebeck effect; a temperature gradient is induced at the junctions between the different metals when a current is applied. The thermal current flows in the opposite direction of the induced electrical current. The direction of the thermal current can be changed by reversing the polarity of the current.[7] As a result, the Peltier effect can be used for either solid state heating or cooling. The Peltier coefficient (π) is calculated by dividing the heat carried by charges (Q) by the current across the junction (I) (Equation (2)).[38] Temperature controlled seats and refrigerators are two devices that utilize the Peltier effect.[37]

$$\pi = \frac{Q}{I} \qquad (2)$$

In 1851, a relationship between the Seebeck and Peltier effects was discovered and described through the Kelvin Relation (Equation (3)).[38] This third thermoelectric effect is known

4

as the Thomson Effect. [8, 34] It was predicted and observed by the Irish mathematical physicist and engineer William Thomson, also known as Lord Kelvin. The Thomson Effect occurs when a current is passed through a material with a temperature gradient. This results in the absorption or production of heat.

$$S = \frac{\pi}{T} \qquad (3)$$

1.2 Thermoelectric Materials and Generators

A thermoelectric (TE) material is defined as a solid state material that converts heat into electricity.[5-7] These materials are used in thermoelectric generators to produce electricity. The TE materials typically used in these devices are n-type and p-type semiconductors.[7] TE materials have been proven to improve energy efficiency though testing in automobiles. However, the most efficient TE materials to this date are comprised of elements that are toxic and/or expensive such as Pb and Te.[64] In addition to toxicity and price, their efficiencies for converting heat into electricity are less than 10%.[1] For that reason, the main object of this project is to develop a TE material that is comprised of less expensive and less toxic elements that provides similar or better energy conversion efficiencies.
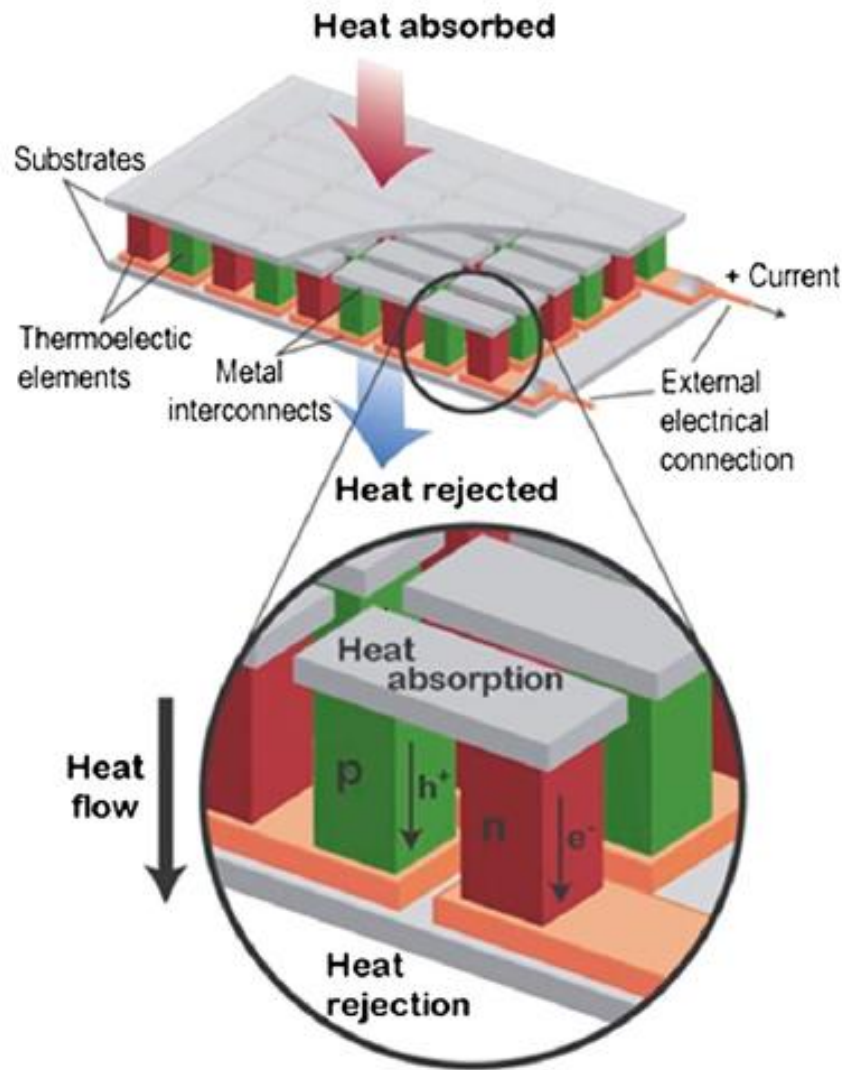
Figure 4: A Typical Thermoelectric Module[2]

1.3 Thermoelectric Efficiency and the Dimensionless Figure of Merit

The efficiency (η) of a thermoelectric generator is dependent on the temperature of the

hot side (T_H) and the temperature of the cold side (T_C). This is referred to as the Carnot term. The

efficiency is also based on the dimensionless figure of merit (ZT) as shown in Equation (4).[1, 3]

$$\eta = \frac{T_H - T_C}{T_H} \frac{\sqrt{1 + ZT} - 1}{\sqrt{1 + ZT} + \frac{T_C}{T_H}} \qquad (4)$$

Therefore, a large temperature gradient and a high ZT result in a high efficiency of power generation. Equation (5) is used to calculate the dimensionless figure of merit for a TE generator.

$$ZT = \frac{(S_p - S_n)^2}{\left[\sqrt{\frac{\kappa_n}{\sigma_n}} + \sqrt{\frac{\kappa_p}{\sigma_p}}\right]^2} T \qquad (5)$$

Where S is the Seebeck coefficient, κ is thermal conductivity, σ is electrical conductivity, and T is absolute temperature. In this expression, the subscripts p and n refer to the p-type and the n-type semiconductor materials used respectively.

The dimensionless figure of merit can be used to describe a material's ability to convert heat into electricity. For a TE material, ZT is

$$ZT = \frac{S^2 \sigma}{\kappa} T \qquad (6)$$

$S^2\sigma$ is known as the power factor (PF) since it is the maximum power a TE material can produce.[46-59] Thermal conductivity of a material is equal to the sum of the electronic contribution to thermal conductivity (κ_e), and the lattice contribution to thermal conductivity (κ_l).[12] The heat carried by electrons is represented in κ_e, where κ_l signifies the heat carried by lattice vibrations. Since electrical resistivity (ρ) is inversely related to electrical conductivity, Equation (6) can be rewritten as in Equation (7):

$$ZT = \frac{S^2}{\rho(\kappa_e + \kappa_l)}T \qquad (7)$$

1.4 Physical Property Interdependence

An effective TE material will have a large Seebeck coefficient, high electrical conductivity (low electrical resistivity) and low thermal conductivity. Unfortunately, all of these parameters are interdependent. The Seebeck coefficient can be calculated using the Mott formula in case of degenerate semiconductors and metals (Equation (8)).[12]

$$S = \frac{8\pi^2 k_B^{\,2}}{3eh^2} m^* T \left(\frac{\pi}{3n}\right)^{\frac{2}{3}} \qquad (8)$$

Where k_B is the Boltzmann constant (1.381×10^{-23} JK^{-1}), e is the charge of an electron (1.602×10^{-19} C), h is Planck's constant (6.626×10^{-34} Js), m^* is the effective mass of the charge carriers, and n is the carrier concentration. Based on this formula, S increases with decreasing carrier concentration. However, by changing the carrier concentration (n), electrical conductivity is affected as shown in Equation (9) where μ is carrier mobility.[1, 12]

$$\sigma = ne\mu \qquad (9)$$

In addition, the electronic contribution to thermal conductivity is related to carrier concentration since it is also related to electrical conductivity. This is shown by the Wiedemann-

Franz Law (Equation (10)), where L is the Lorenz number (its Sommerfeld value being 2.44×10^{-8} WΩK^{-2}).[12]

$$\kappa_e = \sigma LT \qquad (10)$$

Therefore, the Seebeck coefficient, electrical conductivity and thermal conductivity of a material cannot be individually optimized. The relationship between these three properties in addition to the overall effect on *ZT* is illustrated in Figure 5.
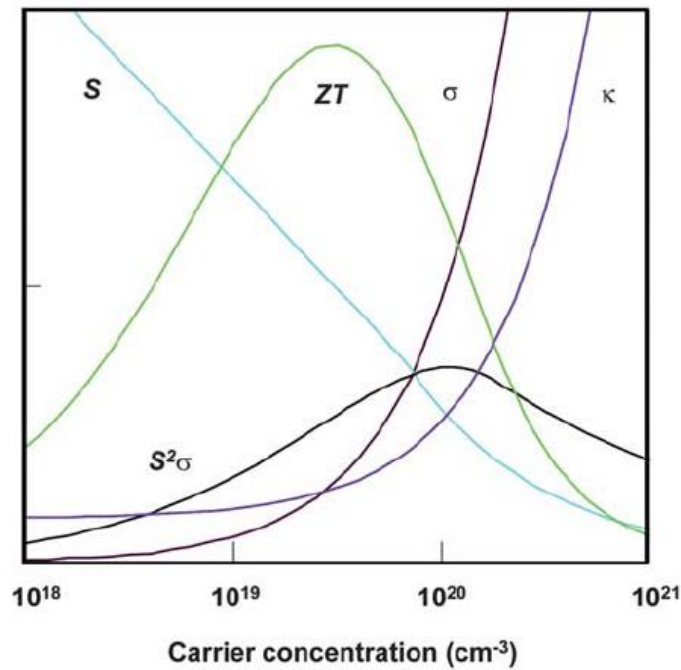
Figure 5: Relationship Between *S*, σ, κ, *PF*, and *ZT* with Respect to Carrier Concentration[12]

Figure 5 also illustrates why semiconductors are the best materials for thermoelectric applications. Insulating materials have large band gaps making it difficult to promote electrons from the valence band to the conduction band. Even at high temperatures, insulators typically

have an empty conduction band and a full valence band. As a result, the carrier concentrations and electrical conductivities of these materials are very low. Although insulators have large Seebeck coefficients and low thermal conductivities, this lack of σ results in ZT values around zero.[1] For metals, n is large since the valence and conduction bands are nearly identical in energy. Therefore, electrons are free to move throughout the bulk of the solid, allowing the σ for these materials to be very large. However, the κ and S for metals are very low giving rise to small ZT's.[1] Hence, insulators and metals are ineffective materials for converting heat into electricity. Semiconductors have carrier concentrations larger than those of insulators but less than those of metals due to their intermediate sized band gaps. For these materials, the band gap is typically lower than 2 eV, and carrier concentrations range from 10^{19} cm^{-3} to 10^{21} cm^{-3}. The figure of merit is maximized for semiconducting materials since they produce a reasonably large S and σ while maintaining a moderately low κ. For that reason, semiconductors are synthesized and studied for thermoelectric research.

1.5 Intrinsic and Extrinsic Semiconductors

There are two types of semiconductors: intrinsic and extrinsic. Intrinsic semiconductors are pure materials with semiconducting properties. Si and Ge are two examples of these kinds of materials. Intrinsic semiconductors that have been doped are known as extrinsic semiconductors. Doping is the process of intentionally adding small amounts of hetero elements that have similar energy levels to that of the host. The purpose of doping is to create an excess of charge carriers. There are two types of extrinsic semiconductors: p-type and n-type. The addition of a dopant with fewer valence electrons than that of the host results in the formation of a p-type semiconductor. An n-type semiconductor is formed when adding a dopant with more valence

10

electrons. $HfCoSb_{0.99}Sn_{0.01}$ and $Mg_2Si_{0.98}Bi_{0.02}$ are an example of a *p*-type and an *n*-type

semiconductor respectively.

With respect to the Seebeck coefficient, *p*-type semiconductors produce positive values

where *n*-type semiconductors produce negative ones. Since positive carriers (holes) are the

dominant charge carriers in *p*-type materials, they migrate from the hot side to the cold side. This

produces a larger voltage at the hot side of the material since electrons travel in the opposite

direction of holes. By using the cold side as a reference point, positive ΔT and ΔV values are

obtained. By using Equation (1), a positive *S* is obtained. On the other hand, *n*-type

semiconductors have electrons as the main form of charge carriers. Therefore, the voltage is

larger at the cold side, resulting in a negative *S*. By adding electrons to a system, a *p*-type

material can be converted to *n*-type. This is illustrated with bismuth telluride in Figure 5. When

the amount of Te is 60%, a positive maximum *S* is obtained. By adding more tellurium, the

Seebeck coefficient decreases and reaches zero at 62.5% Te. Further additions increase the

Seebeck coefficient in the negative direction until an atomic percentage of 64% Te is reached.[40]

Recall from Equation (4) that the *S* is squared for calculating *ZT*. Therefore, a large negative *S* is

useful for producing large figures of merit. Although the best Seebeck coefficients are obtained

at 60% and 64%, the electrical resistivities at these points are also very high (low electrical

conductivity). In general, intrinsic semiconductors exhibit their best Seebeck coefficient while at

the same time having their highest electrical resistivity.
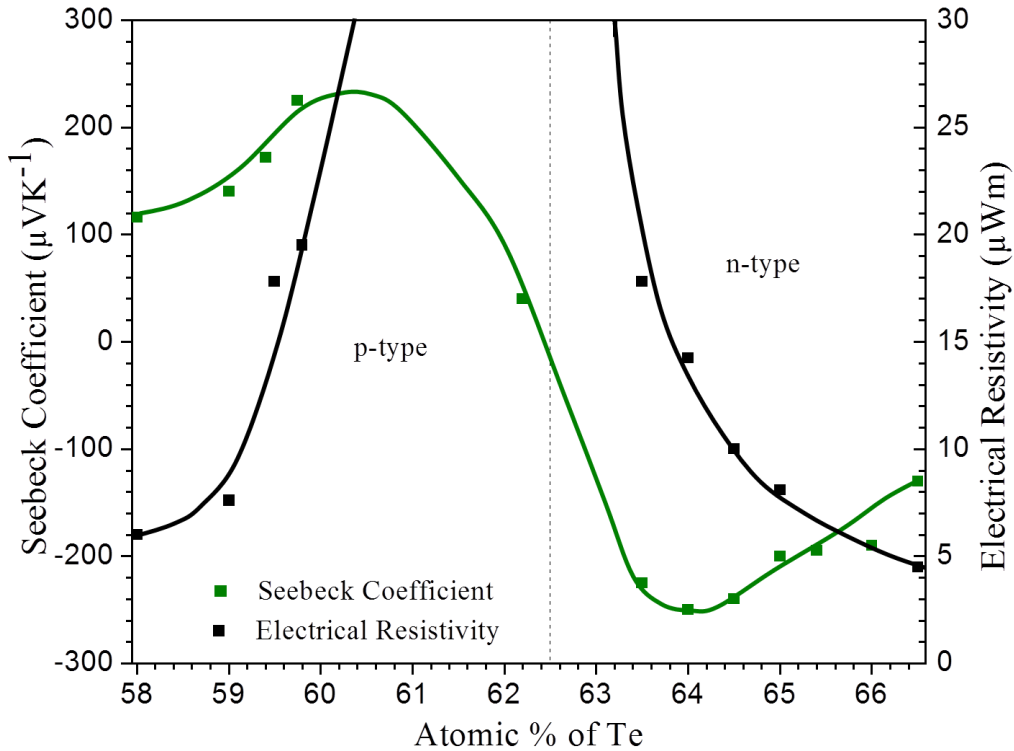
Figure 6: Seebeck Coefficient and Electrical Resistivity of Bismuth Telluride vs. Atomic % of Tellurium at Room Temperature[40]

1.6 Thesis Objectives

In 2001, Q. Shen *et al*. synthesized $Zr_{0.5}Hf_{0.5}Ni_{0.8}Pd_{0.2}Sn_{0.99}Sb_{0.01}$. At that time, this alloy displayed the best thermoelectric properties for ZrNiSn based Half Heusler compounds.[18, 49] By adding ZrO_2 nano-inclusions, L. Chen *et al*. were able to increase *ZT* from 0.56 to 0.75. $Ti_{0.5}Zr_{0.25}Hf_{0.25}NiSn_{0.998}Sb_{0.002}$ currently has the highest reported *ZT* in the literature for a Half Heusler material. A *ZT* of 1.5 was reported for this alloy by N. Shutoh and S. Sakurada in 2003.[19] However, this material was prepared without nano-structuring. Therefore, one main objectives of this project was to synthesize *n*-type $Ti_{0.5}Zr_{0.25}Hf_{0.25}NiSn_{1-x}Sb_x$ and optimize this compound through doping and ZrO_2 nano-inclusions in an attempt obtain a *ZT* higher than 1.5.

Since the highest ZT for p-type materials does not exceed 0.8, synthesizing a more effective material is another goal. In Shutoh and Sakurada's paper, undoped $Ti_{0.5}Zr_{0.25}Hf_{0.25}NiSn$ was synthesized and claimed to exhibit a ZT of 1.28. Therefore, p-type materials that mimic this structure were prepared in an attempt to produce a ZT higher than 0.8. The p-type materials that were synthesized and studied in this project were $Ti_{0.5}Zr_{0.25}Hf_{0.25}Co_xNi_{1-x}Sn$ compounds. Like the n-type materials, the goal was to optimize the physical properties via doping and the addition of ZrO_2 nano-materials. Refer to Section 2.8 of the thesis for more information on the literature results reported for the compounds discussed above.

2.0 Heusler Structures and Physical Properties

2.1 Heusler History

In 1903, a German chemist and mining engineer by the name of Friedrich Heusler discovered a ternary intermetallic with the composition Cu_2MnSn.[13] Friedrich Heusler found that Cu_2MnSn is ferromagnetic at room temperature, even though it is comprised of non-magnetic elements. Compounds that adopt the same structure type are referred to as Heusler compounds. Depending on the elemental composition, these compounds can adopt a variety of different properties such as semiconducting, superconducting, ferromagnetic, etc…

2.2 Heusler Compounds

Compounds with the chemical formula X_2YZ may adopt the Heusler structure type. These materials are also referred to as Full Heusler (FH) compounds since the tetrahedral sites are completely filled. In this formula, X is a transition metal, Y is another transition metal or a rare earth metal, and Z is a p-block element.[14] Cu_2MnAl and Ni_2TiSn are two examples of normal Heusler compounds (Figure 7c). These ternary intermetallics crystallize in a cubic structure with a face centred cubic (fcc) Bravais lattice. Their structures are centrosymmetric and adopt the space group $Fm\overline{3}m$ (space group number 225).[15, 16] The appearance of the Heusler structure can be thought of as the combination of two common crystal structures, namely NaCl and CaF_2 (Figure 7a and 7b). In a normal Heusler compound, the Z atoms form the fcc lattice, the X atoms fill all of the tetrahedral holes, and the Y atoms fill all of the octahedral holes. When referring to the normal Heusler structure type, Cu_2MnAl is used as the prototype.

14
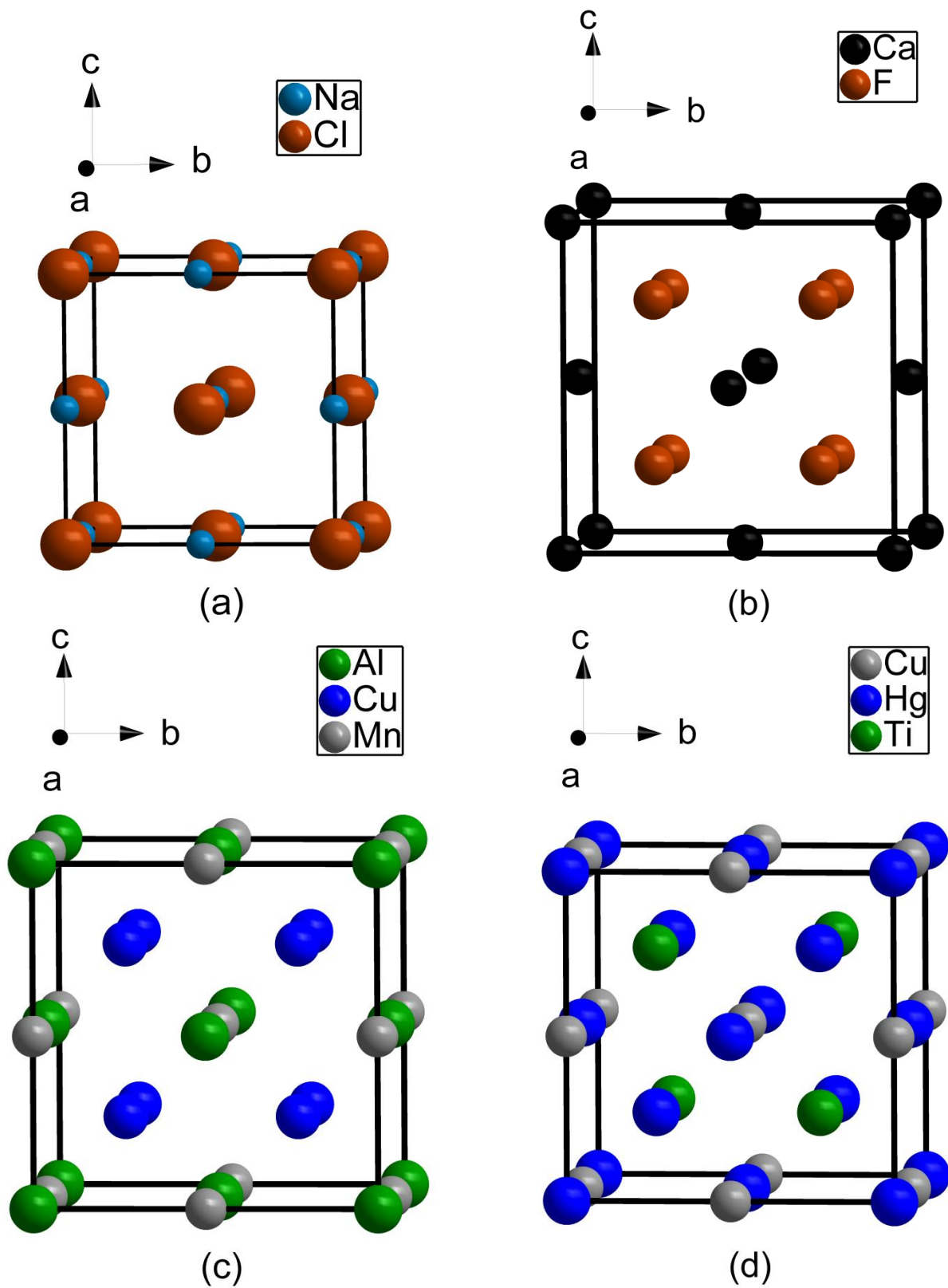
Figure 7: (a) NaCl, (b) CaF$_2$, (c) Heusler prototype Cu$_2$MnAl, and (d) Inverse Heusler prototype

Hg$_2$CuTi crystal structures

15

2.3 Inverse Heusler Compounds

For compounds containing the formula X_2YZ, the placement of atoms within the crystal is dependent on the electronegativity of the X and Y metals. When X is more electronegative than Y, the normal Heusler structure described above is formed. However, when X is more electropositive, an Inverse Heusler is produced.[44] Mn_2CoSn, Mn_2NiGe, and Fe_2CoGa are just a few types of Inverse Heuslers that have been studied in the literature.[44-45] In this case, X forms the fcc lattice and fills half of the tetrahedral holes, Y atoms fill all of the octahedral voids, and the Z element is located in the remaining tetrahedral holes. When filling the tetrahedral holes, atoms of the same kind do not occupy adjacent positions. The Wyckoff positions are 4a (0,0,0) and 4d (¾, ¾, ¾) for X, 4b (½, ½, ½) for Y, and 4c (¼, ¼, ¼) for Z. This atomic arrangement lowers the crystal symmetry due to the removal of the inversion centre. Therefore, Inverse Heuslers are non-centrosymmetric and have the space group $F\overline{4}3m$ (space group number 216). Hg_2CuTi is used as the aristotype when discussing the Inverse Heusler structure (Figure 7d).[45]

2.4 Quaternary Heusler Compounds

When describing Inverse Heusler compounds, $(XY)\,X'Z$ is sometimes used instead of the conventional X_2YZ formula. This is because an X atom can be replaced by another transition metal or an alkali earth metal to form a quaternary Heusler material. PMgTiCo and CoFeMnAl are a couple examples of studied quaternary Heusler compounds. Elements X and Y form a NaCl structure where the X' and Z atoms fill the tetrahedral holes. The X, X', Y, and Z elements are located at Wyckoff positions 4a (0,0,0), 4d (¾, ¾, ¾), 4b (½, ½, ½), and 4c (¼, ¼, ¼) respectively. The prototype for all Quaternary Heusler compounds is LiMgPdSn. Quaternary Heusler crystals have the exact same symmetry as the Inverse Heusler's.

2.5 Half Heusler Compounds

Materials with the chemical composition XYZ are referred to as Half Heusler (HH) compounds. They are named this because the tetrahedral holes in the lattice are half filled. X is typically an alkaline metal, alkaline earth metal, transition metal, or a rare earth metal. The Y element is either a transition metal or a group 13 element, where Z is a *p*-block element.[14] From a visual inspection, the structure of these compounds appears as the combination of two common crystal structures; NaCl and ZnS blende (Figures 8a and 8b). LiAlSi and MgAgAs are both used as archetypes for HH compounds (Figures 8c). HH compounds are similar to Inverse Heusler and Quaternary Heusler's as they also adopt a non-centrosymmetric crystal structure with a $\bar{F4}$ 3*m* space group.
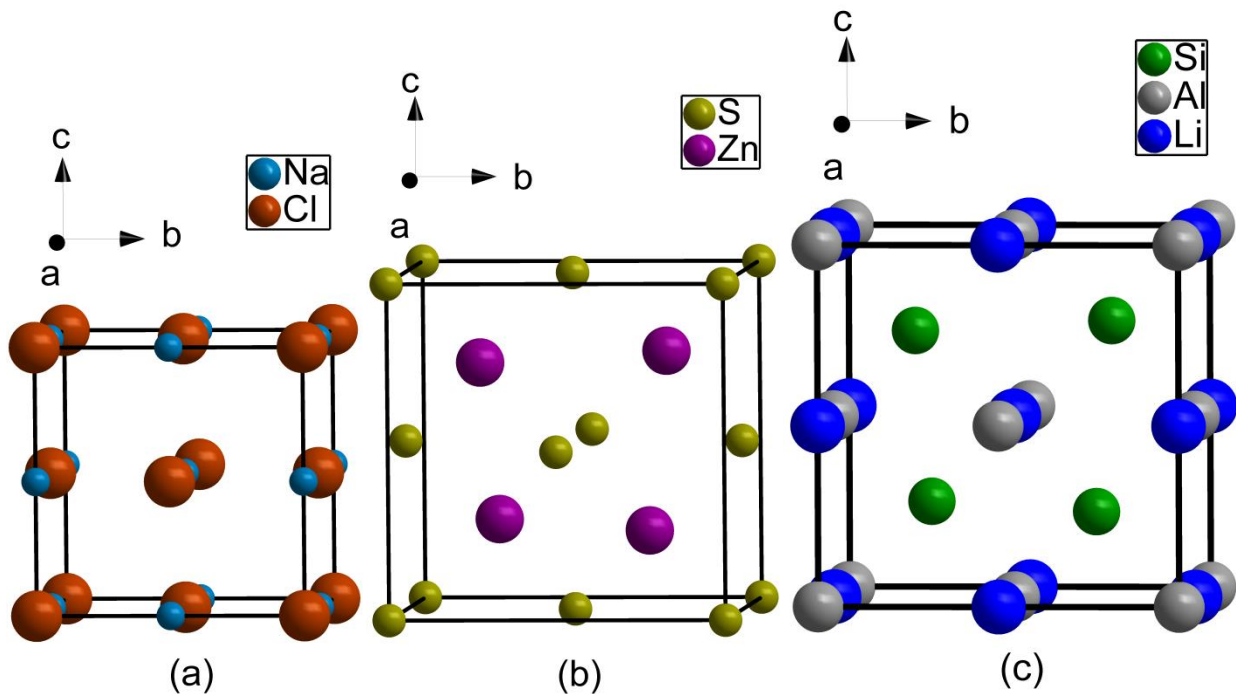
Figure 8: (a) NaCl, (b) ZnS Blende and (c) the HH Prototype LiAlSi Crystal Structures

The placement of atoms within the unit cell is dependent on the relative size difference between elements X and Y. If these metals show little difference in their sizes, X atoms occupy octahedral sites where elements Y and Z form covalent bonds to construct a ZnS blende network. In this case, X fills all the octahedral holes [Wyckoff position 4b (½, ½, ½)], Y forms the fcc lattice [Wyckoff position 4a (0, 0, 0)] and the Z anions fill half of the tetrahedral holes [Wyckoff position 4c (¼, ¼, ¼)], where each anion is coordinated by eight cations. LiAlSi, MgAgAs, and LiMgSb are all examples of HH intermetallics that adopt this atomic placement. Although both prototypes used for Half Heusler compounds implement this arrangement, a large portion of HH materials studied in literature do not. TiNiSn, LnPdBi, HfCoSb, and ErNiSb are just a few HHs that have been studied in the literature and do not crystallize the same as the archetypes. In each of the four compounds listed above, the two metals vary significantly in atomic size. For this case, the Y atoms occupy the tetrahedral positions where X and Z form a NaCl network. Therefore, X, Y, and Z atoms occupy the Wyckoff positions, 4b (½, ½, ½), 4c (¼, ¼, ¼) and 4a (0, 0, 0) in that order. This structure type is typically formed when the compound consists of two transition metals, or a transition metal and a rare earth metal.

2.6 Magnetic Properties

To reiterate, FH and HH compounds can exhibit a variety of properties depending on the elements that compose them. The next few sub-sections will briefly describe some of the properties that have been reported in the literature. However, since the scope of this project is to measure and optimize the thermoelectric properties of HH phases, all other properties are omitted in section "4.0 Results" of the thesis.

Magnets are used in a variety of applications in everyday life. They can be found in memory storage devices, refrigerators, speakers, compasses etc. Both FH and HH compounds can display various magnetic properties depending on the elements that comprise them.

To restate, in 1903 Friedrich Heusler discovered that Cu_2MnSn displays ferromagnetism. In a ferromagnet, all magnetic moments align parallel in a cooperative effect when an external magnetic field is applied. Since Friedrich Heusler's discovery, a variety of ferromagnetic FH materials have been synthesized, such as Cu_2MnAl, Co_2MnGa, Ni_2MnGa and Co_2MnSi.[13, 26, 31-32] Ferromagnetism has also been observed in HH compounds like NdNiSb, VCoSb and PdMnSb.[42] A half-metallic ferromagnetic is a material that performs like a metal for one spin direction and as an insulator for the other. Mn_2VAl and Co_2FeSi are two examples of FH materials have been claimed to adopt this property. For HH compounds, half-metallic ferromagnetism is generally observed in compounds containing manganese (ex. MnNiSb and MnPtSb). Antiferromagnetism has also been observed in both FH and HH materials. In antiferromagnetic materials, the magnetic moments align antiparallel when exposed to an external magnetic field. This magnetic property is typically observed in rare earth containing HH compounds. Cu_2MnSb, Ru_2MnGe, HoPdBi, NdBiPt are all examples of materials within the Heusler family that have been reported to display antiferromagnetism.[13, 27-30]

The magnetic moment varies depending on the number of valence electrons (N_V) for materials within the Heusler family. Equations (11) and (12) can be used to estimate the magnetic moments of FH and HH materials respectively. The highest magnetic moment from a FH material was reported for Co_2FeSi as $5.97\mu_B$ at 5 K.[42]

$$m_{X_2YZ} = N_V - 24 \qquad (11)$$

$$m_{XYZ} = N_V - 18 \qquad (12)$$

2.7 Superconducting Properties

A superconductor is a material that conducts electricity with zero resistance when below a critical temperature (T_c). A few of their applications include, creating larger magnetic fields in nuclear magnetic resonance instruments, and reducing (nearly eliminating) friction in transport vehicles. In 1982, Ishikawa *et al*. discovered the first superconducting FH materials, Pd_2RESn and Pd_2REPb.[42] Superconductivity is generally observed in FH compounds with 27 valence electrons. Although many FH superconductors have been reported in the literature, critical temperatures are too low from an application stand point. The highest T_c for a FH compound was observed in Pd_2YSn and reported as 4.9 K. The only HH material claimed in literature to adopt superconducting properties is LaPtBi, which has a T_c of 0.9 K.[42] Although superconductors have many applications, they are useless in thermoelectrics because they produce *ZT* values of zero since $S = 0$.[41]

2.8 Thermoelectric Properties

Semiconductors are typically used as TE materials because they provide optimum figure of merits. Semiconducting FH materials generally have valence electron counts of 24 per formula unit, while Half Heuslers have 8 or 18. A few examples include Fe_2VAl, Fe_2TiSn, TiNiSn and HfCoSb.[46-48] HH materials have attracted a lot of attention in the thermoelectric community due to their ability to produce large power factors. However, they can also exhibit

large values of thermal conductivity, making it challenging to produce a meaningful figure of merit.[43, 50]

2.8.1 Full Heusler TE Properties

Fe$_2$VAl based FH materials have been thoroughly studied in the literature for their TE properties.[42, 47-48] At 300 K, Fe$_2$VAl exhibits an σ, S, and κ of approximately 1350 $\Omega^{-1}cm^{-1}$, 25 μVK^{-1} and 28 W m$^{-1}K^{-1}$ respectively.[47] As a result, this intermetallic produces a PF of about 0.8 μW cm$^{-1}K^{-2}$ and a very low ZT_{max} ($\approx$ 0.001). However, these properties can be significantly enhanced through doping.

In 2006, Y. Nishino et al. investigated and optimized the TE properties of Fe$_2$VAl$_{1-x}$Ge$_x$.[47] By doping Al with Ge, the TE properties were improved dramatically. Y. Nishino et al. observed a significant improvement and a change in the sign of the Seebeck coefficient when doping with Ge. For example, $S \approx$ -120 μVK^{-1} at 300 K for Fe$_2$VAl$_{0.9}$Ge$_{0.1}$. Improvements in both electrical and thermal conductivity were observed from this addition. At 300 K, $\sigma \approx$ 4000 $\Omega^{-1}cm^{-1}$, $\kappa \approx$ 14 W m$^{-1}K^{-1}$ for Fe$_2$VAl$_{0.9}$Ge$_{0.1}$. The increase in both S and σ increased the PF to 59 μW cm$^{-1}K^{-2}$.[47] Although significant enhancements were made to the TE properties, a maximum figure of merit (ZT_{max}) of only 0.13 was achieved at 300 K for Fe$_2$VAl$_{0.9}$Ge$_{0.1}$.

In 2012, M. Mikami et al. studied the effects of doping the vanadium site of Fe$_2$VAl with tungsten. Similar to Y. Nishino et al. findings, significant improvements in σ, S, and κ were observed through doping. M. Mikami et al. reported a ZT_{max} of 0.20 for Fe$_2$V$_{0.9}$W$_{0.1}$Al at 400

K.[48] The approximate values of S, σ, κ at this temperature are -120 μVK^{-1}, 2220 $\Omega^{-1}cm$, and 5.5 W $m^{-1}K^{-1}$ respectively.

2.8.2 Half Heusler Thermoelectric Properties from *n*-type Materials

The best TE properties for *n*-type HH compounds have been reported for MNiSn (M = Ti, Zr, Hf) materials. These materials display high power factors. For instance, ZrNiSn exhibits an σ $\approx$ 550 $\Omega^{-1}cm^{-1}$ and $S \approx$ -165 μVK^{-1} at 900K resulting in a $PF \approx$ 15 $\mu W\ cm^{-1}K^{-2}$.[49] However, high figures of merit are not observed in ternaries due to high thermal conductivity. At 900K, ZrNiSn has a $\kappa \approx$ 6.50 W $m^{-1}K^{-1}$ resulting in a $ZT_{max} \approx$ 0.21. As mentioned previously, thermal conductivity is the sum of the electrical and lattice contributions. Since κ_e is related to σ, researchers often focus on decreasing κ_l to increase ZT. One strategy for lowering κ_l is through partial substitutions with another element that has the same number of valence electrons but a different mass. This process is referred to as "mass fluctuation". Partially substituting Hf for Zr in ZrNiSn causes κ_l to lower, resulting in an increase in ZT. For example, the total thermal conductivity for $Zr_{0.5}Hf_{0.5}NiSn$ at 693 K is approximately 4.10 W $m^{-1}K^{-1}$. This causes ZT_{max} to rise to approximately 0.53.[19] As shown below in Equation 13, κ_l is proportional to the specific heat of the lattice (C_v), the sound velocity (v_s), and the phonon mean free path (λ_{ph}), which gets reduced by mass fluctuations by more phonon scattering.

$$\kappa_L = \frac{1}{3}C_v v_s \lambda_{ph} \qquad (13)$$

In 2003, N. Shutoh and S. Sakurada synthesized and optimized the TE properties of semiconducting $Ti_x(Zr_{0.5}Hf_{0.5})_{1-x}NiSn_{1-y}Sb_y$ HH materials. The figure of merit was first

optimized through mass fluctuation. It was determined that $Ti_{0.5}Zr_{0.25}Hf_{0.25}NiSn$ displays the best

TE properties for the undoped samples. N. Shutoh and S. Sakurada claimed a ZT_{max} of 1.28 at

693 K for this compound. The approximate values of σ, S for $Ti_{0.5}Zr_{0.25}Hf_{0.25}NiSn$ at this

temperature are 510 $\Omega^{-1}cm^{-1}$, and -335 μVK^{-1} respectively. This computes to an approximate PF

of 57 $\mu\,Wcm^{-1}K^{-2}$. N. Shutoh and S. Sakurada did not provide κ values at 693 K. However, they

did provide values at 773 K, which is approximately 3.10 W $m^{-1}K^{-1}$ for the undoped alloy.

Further optimizations in ZT were accomplished through successful doping with Sb. N. Shutoh

and S. Sakurada reported a ZT_{max} of 1.5 at 693 K for $Ti_{0.5}Zr_{0.25}Hf_{0.25}NiSn_{0.998}Sb_{0.002}$. This is the

highest figure of merit reported to date for a HH compound.[19] $Ti_{0.5}Zr_{0.25}Hf_{0.25}NiSn_{0.998}Sb_{0.002}$

shows $\sigma \approx 665\ \Omega^{-1}cm^{-1}$ and $S \approx$ -310 μVK^{-1} ($PF \approx 64\ \mu W\ cm^{-1}K^{-2}$) at 693 K, and $\kappa \approx 2.95$ W $m^{-1}K^{-1}$ at 773 K. The figure of merit as a function of temperature for this and other doped

semiconductors is shown in Figure 9.
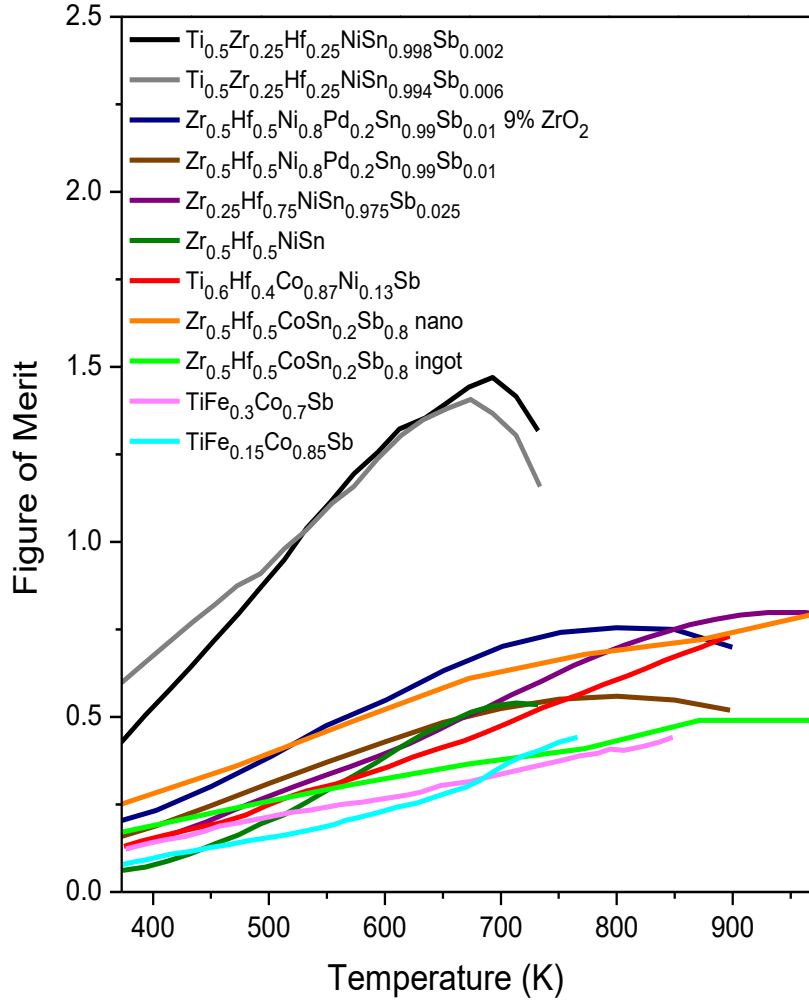
Figure 9: Thermoelectric Figure of Merit of HH Materials from the Literature[18-20, 23-24, 42]

In 2005, L. Chen *et al.* optimized the properties of $Zr_{0.5}Hf_{0.5}Ni_{0.8}Pd_{0.2}Sn_{0.99}Sb_{0.01}$. At 800 K, this semiconductor outputs an $\sigma \approx 1060$ $\Omega^{-1}cm^{-1}$, $S \approx -154$ μVK^{-1} ($PF \approx 25$ μW $cm^{-1}K^{-2}$) and $\kappa \approx 3.60$ W $m^{-1}K^{-1}$, resulting in a $ZT_{max} \approx 0.56$. The figure of merit for this material was additionally enhanced by incorporating ZrO_2 nano-particles. These nano-inclusions are spread randomly throughout the material and act as additional phonon scattering centres to lower κ_l.[18] By forming composites, the number of grains within the material grows. This causes the number of grain boundaries to increase resulting in more phonon scattering. Since phonons are scattered

more easily, the distance they travel before a collision (ie. λ_{ph}) is lowered. Hence, κ_l and total

thermal conductivity are decreased. By adding 9 volume percent (vol-%) of ZrO_2 to

$Zr_{0.5}Hf_{0.5}Ni_{0.8}Pd_{0.2}Sn_{0.99}Sb_{0.01}$, L. Chen *et al*. were able to decrease κ to approximately 2.60 W m^{-1}K^{-1} at 800 K. Although adding more grain boundaries can lower κ_l, it can also cause electrons to

scatter, resulting in a decrease in electrical conductivity. By adding the ZrO_2 particles, σ was

reduced to a value around 880 Ω^{-1}cm^{-1}. However, *ZT* improved since the overall decrease in κ is

much more significant than that in σ. L. Chen *et al*. reported a *ZT*$_{max}$ of 0.75 for

$Zr_{0.5}Hf_{0.5}Ni_{0.8}Pd_{0.2}Sn_{0.99}Sb_{0.01}$ with 9 vol-% ZrO_2 added. *ZT* vs. temperature for the materials

described above are plotted in Figure 9. Table 1 illustrates a variety of physical properties

reported in the literature for *n*-type Half Heusler compounds.

Table 1: Approximate Physical Property Values for *n*-type Half Heusler Materials from

Literature

Sample	σ (Ω^{-1}cm^{-1})	S (μVK^{-1})	κ (W m^{-1}K^{-1})	T (K)	ZT_{max}
$Zr_{0.5}Hf_{0.5}Ni_{0.8}Pd_{0.2}Sn_{0.99}Sb_{0.01}$ (0 vol-% ZrO_2)[18]	1060	-154	3.60	800	0.56
$Zr_{0.5}Hf_{0.5}Ni_{0.8}Pd_{0.2}Sn_{0.99}Sb_{0.01}$ (3 vol-% ZrO_2)[18]	995	-153	3.41	800	0.55
$Zr_{0.5}Hf_{0.5}Ni_{0.8}Pd_{0.2}Sn_{0.99}Sb_{0.01}$ (6 vol-% ZrO_2)[18]	1015	-165	3.05	800	0.72
$Zr_{0.5}Hf_{0.5}Ni_{0.8}Pd_{0.2}Sn_{0.99}Sb_{0.01}$ (9 vol-% ZrO_2)[18]	880	-167	2.60	800	0.75
$Zr_{0.5}Hf_{0.5}NiSn$[19]	450	-240	4.10 (at 773K)	693	0.53
$Ti_{0.5}Zr_{0.25}Hf_{0.25}NiSn$[19]	510	-335	3.10 (at 773K)	693	1.28
$Ti_{0.5}Zr_{0.25}Hf_{0.25}NiSn_{0.998}Sb_{0.002}$[19]	665	-310	2.95 (at 773K	693	1.50
$Ti_{0.6}Hf_{0.4}Co_{0.87}Ni_{0.13}Sb$[23]	633	-190	2.95	900	0.70

2.8.3 Half Heusler TE Properties from *p*-type Materials

The TE properties of *p*-type semiconducting HH reported in the literature have not been able to match those for obtained for *n*-type. For example, in 2007 Kawano *et al*. synthesized *p*-type based ErNiSb HH materials and obtained a ZT_{max} of 0.19 and 0.29 for undoped ErNiSb and doped ErNiSn$_{0.01}$Sb$_{0.99}$ respectively.[25] These properties were the result of *PF*'s lower than 20 μW cm^{-1}K^{-2} and κ higher than 4 W m^{-1}K^{-1}.

The p-type $Zr_{0.5}Hf_{0.5}CoSb_{0.8}Sn_{0.2}$ HH was first synthesized in 2008 by S. R. Culp *et al.* and reported to exhibit a *ZT$_{max}$* of 0.50 at 1000 K.[54] X. Yan *et al.* were able to significantly enhance these properties in 2010. This was accomplished by nano-structuring through the use of ball-milling. Ball-milling increases the number of grain boundaries in a material by reducing the average grain size. This results in more interfaces which cause phonons to scatter.[20] Therefore, nano-structuring is used to enhance TE properties by decreasing total thermal conductivity through reductions in κ_l.[39] Similar to the use of nanoinclusions, nano-structuring can slightly lower σ due to electron scattering, e.g. at the increased interfaces. However, the decrease in κ_l is often more substantial, causing *ZT* to rise. X. Yan *et al.* synthesized bulk samples and ball-milled samples of $Zr_{0.5}Hf_{0.5}CoSb_{0.8}Sn_{0.2}$. At 973 K, $\kappa \approx 4.88$ W m^{-1}K^{-1} and $\kappa_l \approx 3.68$ W m^{-1}K^{-1} for bulk samples. The ball-milled samples showed significantly better properties at the same temperature since $\kappa \approx 3.25$ W m^{-1}K^{-1} and $\kappa_l \approx 2.18$ W m^{-1}K^{-1} were obtained.[20] σ and S for the ball-milled sample at 973 K are 568 Ω^{-1}cm^{-1} and 217 μVK^{-1} in that order. This resulted in a maximum *ZT* of 0.8; a 60% improvement from the original value of 0.5. This is the highest figure of merit reported for a p-type HH material. *ZT* vs. temperature for both the ingot and ball-milled samples are displayed in Figure 9. Table 2 shows TE properties reported in the literature for p-type HH materials.

Table 2: Approximate Physical Property Values for *p*-type Half Heusler Materials from

Literature

Sample	σ ($\Omega^{-1}cm^{-1}$)	S (μVK^{-1})	κ (W m^{-1}K^{-1})	T (K)	ZT_{max}
$Zr_{0.5}Hf_{0.5}CoSb_{0.8}Sn_{0.2}$ (ingot)[20]	635	195	4.88	973	0.50
$Zr_{0.5}Hf_{0.5}CoSb_{0.8}Sn_{0.2}$ (ball-milled)[20]	568	217	3.25	973	0.80
$TiFe_{0.15}Co_{0.85}Sb$[24]	250	303	4.33	850	0.45
$ErNiSn_{0.01}Sb_{0.99}$[25]	550	180	4.07	669	0.29

3.0 Experimental Equipment and Sample Characterization

3.1 Synthesis Equipment

Since the elements used in this project are sensitive to oxygen, syntheses must be performed in an inert atmosphere. As a result, all samples were prepared inside a glove box (Figure 10) under argon atmosphere. Stoichiometric amounts of each element were weighed, combined and homogenized using a mortar and pestle.

Figure 10: Argon-Filled Glove Box

After homogenizing elements in the glove box, samples were loaded into the cold press

and pelletized using the Weber-Pressen (Figure 11). 6 mm diameter pellets were formed by

applying a force of 20 kN (~ 700 MPa) for at least 20 minutes.

Figure 11: The Cold-Press (Weber-Pressen)

Arc melting was used as the main synthesis technique for all samples. Cold-pressed pellets were placed on a copper block and loaded into the arc-melter (Figure 12). This instrument uses a tungsten electrode and can heat samples up to 2800 K for approximately 40 seconds. A large current of approximately 75 A was used for arc melting all samples. Before loading the samples, the Cu block was cleaned with nitric acid to remove surface oxides. During and prior to melting, oxygen was removed and prevented from entering the system by pumping in a constant flow of argon gas. However, it is possible for small traces of oxygen to remain present in the reaction vessel. These traces were removed by arc melting a piece of solid zirconium before the samples. Since oxidation occurs much faster at higher temperatures, any oxygen present in the system will react with zirconium to form ZrO_2; hence, producing an inert atmosphere. Samples were heated for approximately 5 seconds since sample loss increases with arc melting time. Also, too much thermal stress can cause samples to burst into several small pieces. Samples were melted twice (once on each side) to ensure homogeneity.

Figure 12: The Arc-Melter

Samples are not completely pure after arc melting due to the presence of unwanted side products. As a result, samples require further annealing in an inert atmosphere to make them pure. To produce an inert atmosphere, samples were placed into silica tubes which were attached to a vacuum line (Figure 13) and evacuated to pressures on the order of 10^{-4} mbar. The tubes were sealed using a hydrogen-oxygen torch which produces a flame around 2000 K. All samples were annealed in manually controlled furnaces for at least a week.

(a)	(b)	(c)
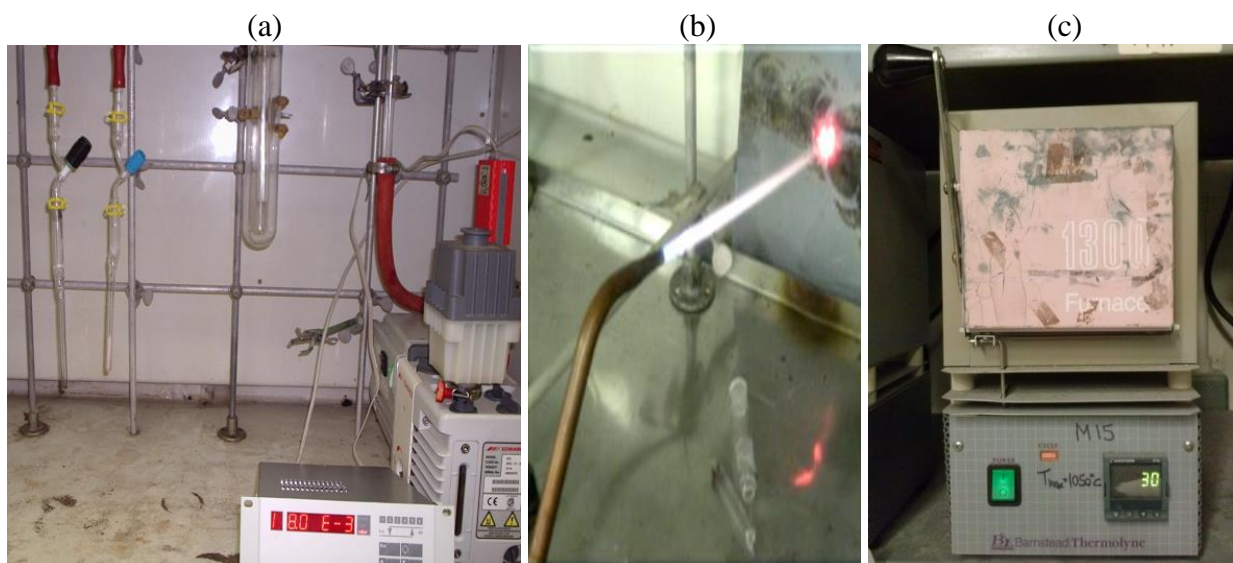
Figure 13: (a) Vacuum Line (b) Hydrogen-Oxygen Torch (c) Manual Furnace

3.2 Purity Characterization

3.2.1 Powder X-ray Diffraction

Powder X-ray Diffraction (PXRD) was run on all samples to analyse phase purity. The INEL XRG 3000 Powder Diffractometer (Figure 14) was used. X-rays are generated by bombarding a metal target with high energy electrons. The INEL XRG 3000 Powder Diffractometer uses a tungsten filament to generate electrons and a copper target for X-ray

production. For all measurements, the voltage and current of the electrons used to bombard the copper target was 30 kV and 30 mA respectively. When X-rays are produced, the wavelengths and intensities of the photons vary.[34] A germanium single crystal is used as a monochromator to produce a single wavelength of 1.5406 Å. These X-rays pass through a collimator where the beam size is adjusted, and then they interact with the sample. The electrons from the atoms within the sample cause the X-rays to scatter. More electrons (i.e higher atomic number) cause more scattering.
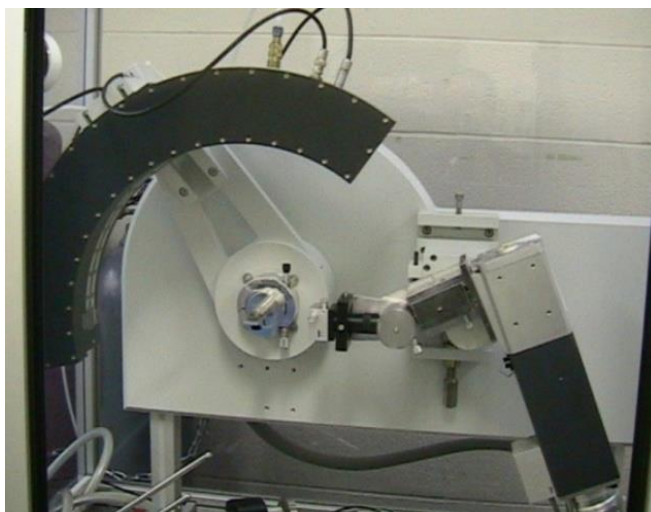
Figure 14: The INEL XRG 3000 Powder Diffractometer

All samples were run on the INEL XRG 3000 Powder Diffractometer for at least 20 minutes to determine sample purity. Purity was analyzed by using a crystallographic database containing known phases and comparing them to the measured diffraction patterns. Diffraction patterns were analysed on the "MATCH!" program, and a database was created by taking known literature diffraction patterns from the "FindIt" program.

3.2.2 Scanning Electron Microscopy and Energy Dispersive X-ray Spectroscopy

Scanning electron microscopy (SEM) is a technique used for obtaining sample images on a micrometer scale for surface topography analysis. In this form of microscopy, samples are struck with a high energy electron beam that typically ranges from $10 - 30$ kV.[8, 36-37] The incoming electrons interact with and eject outer electrons from the sample. Sample images are gathered from the detection of the scattered electrons.

Sample compositions can be acquired through energy dispersive x-ray (EDX) spectroscopy. EDX spectroscopy involves the use of an electron beam that is similar in energy to that used in SEM. In addition to scattering outer electrons, the beam is also capable of removing core electrons due to the large energy. When a core electron is removed, an electron from a higher energy level drops to fill the void. This results in the release of a photon in the form of an x-ray. The energy of this photon is proportional to the energy gap between the two shells. Since each element emits an x-ray with a unique energy, elements within samples can be characterized by their detection. The ratios of the elements within a sample are determined by the relative intensities of the x-rays.

Sample images and elemental compositions were obtained by performing SEM in conjunction with EDX spectroscopy. All measurements were conducted on the Quanta FEG 250 (Figure 15). Since all samples were comprised of heavy elements (ie. Sn, Hf), a 30 kV electron beam was used.

Figure 15: The Quanta FEG 250

3.3 Pelletizing Methods

Once samples are deemed pure via PXRD, thermal conductivity, electrical conductivity, and Seebeck coefficient can be measured. However, these physical property measurements can only be performed on samples in pellet form. Cold-pressing, hot-pressing (HP), and Spark Plasma Sintering (SPS) are three techniques that can be used to create pellets.

For physical property analyses, all samples were pressed via HP with the Oxy-Gon High

Temperature and Press System (Figure 16). This instrument is capable of pressing samples under

a weight of up to 30 tons, and it can heat samples up to 1873 K.[8] To completely remove oxygen

from the system, the chamber is first evacuated to a pressure of around 2×10^{-6} MPa, and then

filled with argon. All samples were pressed into cylindrical pellets using a pair of plungers and a

dye made of graphite.

Figure 16: (a) Oxy-Gon High Temperature and Press System

SPS is similar to HP since both methods involve heating the sample while pressing.

However, samples are heated with heating elements for HP, where SPS heats the sample by

passing a current through it. A pulsed direct current on the order of 1000 A is typically used

when SPS. The dies used for SPS contain a small hole where a thermometer is placed in to

measure the temperature (Figure 17).
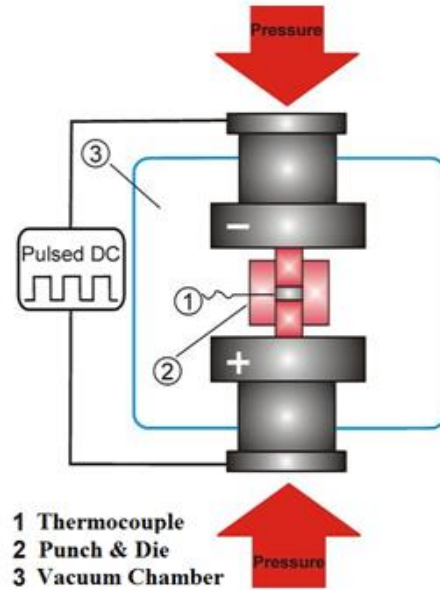
Figure 17: Spark Plasma Sintering Scheme

3.4 Thermal Measurements

A material's thermal conductivity is the product of its thermal diffusivity (α), density (ρ_d), and specific heat capacity (C_p).[52] In this project, Equation (14) was used for calculating the thermal conductivity of all samples.

$$\kappa = \alpha \rho_d C_p \qquad (14)$$

All thermal diffusivity measurements were carried out with the Flash Line 3000 Thermal Diffusivity System (Figure 18). This instrument requires a cylindrical pellet with an approximate diameter of 12.5 mm for analysis. To prevent sample oxidation, the chamber is evacuated and then filled with Ar. This instrument operates by flashing with a Xenon lamp on the sample while measuring the temperature increase on the opposite face with an Infrared detector. The time it

takes the opposite face to reach half its maximum temperature increase ($t_{0.5}$), and the sample

thickness (t) are both used to calculate thermal diffusivity (Equation (15)).[8]

$$\alpha = 0.1388 \frac{t^2}{t_{0.5}} \qquad (15)$$

Archimedes' principle was employed when determining the density of every sample.

Using an analytical balance, samples were weighed in air (w_a) and in water (w_w). The

temperature of the water was also measured to obtain an accurate value for the density of water

(ρ_w). Sample density was then calculated using Equation (16).

$$\rho_d = \frac{w_a(\rho_w - 0.0012 \; gcm^{-3})}{0.99983(w_a - w_w)} + 0.0012 \; gcm^{-3} \qquad (16)$$

A materials specific heat capacity can be measured via Differential Scanning

Calorimetry. However, by knowing the average molar mass of the sample (M_{avg}) and the ideal

gas constant (R), the Dulong-Petit Law (Equation (17)) can be utilized to estimate this value.[8]

Since it has been proven as an accurate approximation, the Dulong-Petit Law was used for

determining the C_p of all samples.

$$C_p = \frac{3R}{M_{avg}} \qquad (17)$$

Figure 18: Flash Line 3000 Thermal Diffusivity System

The Seebeck coefficient and electrical conductivity can be measured simultaneously on the ULVAC-RICO ZEM-3 (Figure 19a). However, this instrument requires a rectangular pellet with a length of 6 – 20mm for analysis. As a result, samples were cut with the Diamond Wheel Saw Model 650 (Figure 19b) to prepare for this measurment.[8]

Figure 19: (a) ULVAC-RICO ZEM-3 (b) Diamond Wheel Saw Model 650

To measure the physical properties, samples were mounted vertically on an electrode in the furnace chamber of the ULVAC-RICO ZEM-3. This chamber was evacuated and then flushed with argon to prevent sample oxidation. Two thermocouples were placed in such a way that they came into contact with two opposing faces of the sample. At a given temperature, the instrument would apply a current (I) through the sample. The voltage (V) was measured, and the resistance (R) was calculated using Ohm's Law (Equation (18)).

$$R = \frac{V}{I} \qquad (18)$$

Prior to analysis, the cross sectional area of the squared end of the pellet (A) and the length between the two thermocouples (L) were measured. The instrument calculated electrical resistivity using Equation (19). As mentioned previously, σ is inversely proportional to ρ.

$$\rho = \frac{RA}{L} \qquad (19)$$

Following ρ measurements, a temperature gradient is applied to one side of the pellet. The Seebeck coefficient is then calculated by measuring the voltage difference at the two sides of the pellet and applying Equation (1).

4.0 Results

4.1 Synthesis

4.1.1 Titanium Antimonide Synthesis

To reiterate, one main goal of this project was to synthesize $Ti_{0.5}Zr_{0.25}Hf_{0.25}NiSn_{1-x}Sb_x$

materials. However, antimony has a boiling point of 2023 K. As a result, elemental Sb would

vaporize when arc melted, affecting stoichiometry. Y. Zhu prepared $TiFe_{1-x}Ni_xSb$ HH

compounds by using $TiSb_2$ as a starting material.[9] The synthesis of $M'Sb_2$ (M' = Ti, Zr, Hf, Nb)

binaries has been discussed by H. Kleinke.[21] These antimonides can be formed by heating

stoichiometric amounts of each element in silica tubes at 923 K for 3-7 days.[21] $TiSb_2$ was

successfully synthesized as illustrated by the pure PXRD pattern (Figure 20). The binary was

prepared by heating powders at 923 K for 3 days, followed by homogenizing and re-heating at

923 K for another 6 days.
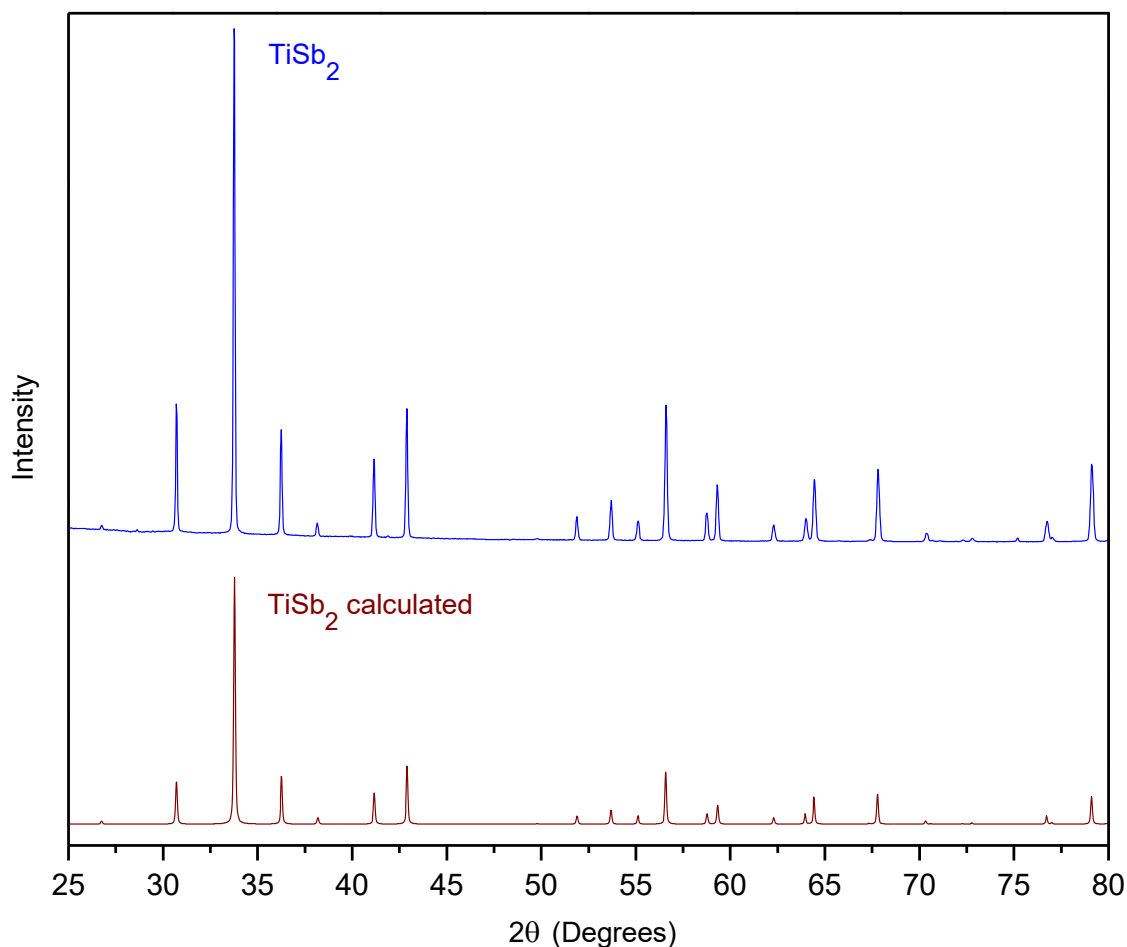
Figure 20: PXRD of a TiSb$_2$ Sample (Sample at the Top, Reference at the Bottom)

4.1.2 Ti$_{0.5}$Hf$_{0.5}$NiSnSb$_{0.04}$ Synthesis Attempts

Synthesis attempts on preparing 5 mmol Ti$_{0.5}$Hf$_{0.5}$NiSn$_{0.96}$Sb$_{0.04}$ samples were carried out

as a starting point for this project. TiFe$_{1-x}$Ni$_x$Sb compounds were synthesized by Y. Zhu by

pressing TiSb$_2$, Ti, Fe, and Ni into a pellet, arc melting them, and annealing at 1073 K in silica

tubes for one week.[9] When using this method for Ti$_{0.5}$Hf$_{0.5}$NiSn$_{0.96}$Sb$_{0.04}$, many side products

were observed in the PXRD plot (Figure 21a). T. Katayama *et al.* stated that TiNiSn was formed

by arc melting several times and annealing at 1073 K for two weeks.[22] In an attempt to purify the

41

Ti$_{0.5}$Hf$_{0.5}$NiSn$_{0.96}$Sb$_{0.04}$ sample mentioned above, it was annealed for another week at 1073 K.

However, the results were unsuccessful as the PXRD pattern still showed side products (Figure

21b). Synthesis attempts were also carried out on preparing Ti$_{0.5}$Hf$_{0.5}$NiSn$_{0.96}$Sb$_{0.04}$ using

Katayama's method. In this method, samples are arc melted four or six times (twice or three

times on each side) and annealed at 1073 K for 2 weeks.[22] The results were unsuccessful as side

products were detected in the plots obtained through PXRD (Figure 21c).
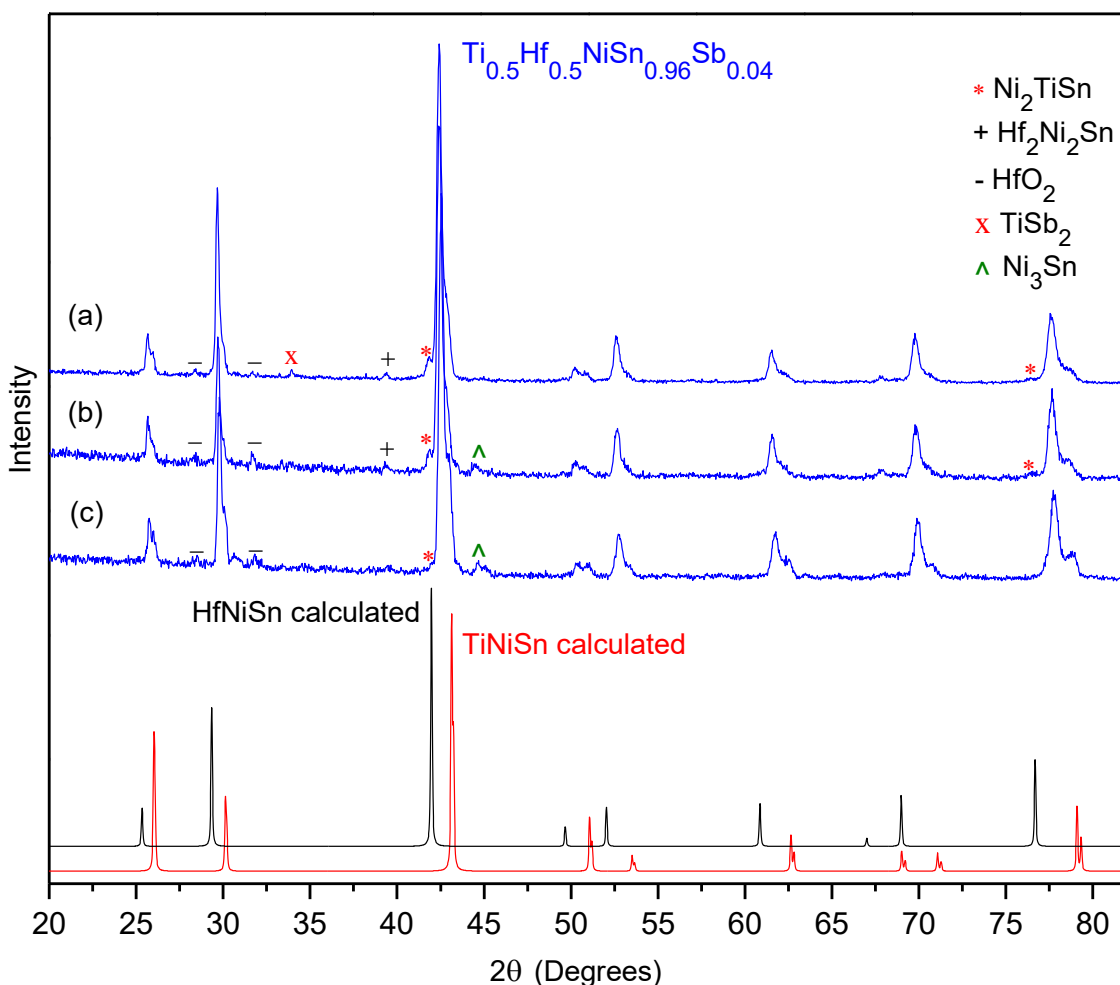

Figure 21: PXRD plots of Ti$_{0.5}$Hf$_{0.5}$NiSn$_{0.96}$Sb$_{0.04}$ samples prepared by (a) Y. Zhu's Method (b)

Y. Zhu's Method with additional annealing for 1 week at 1073 K (c) T. Katayama's method[9, 22]

4.1.3 Ternary Synthesis

To see if the arc melting methods mentioned are effective for making HH materials, TiNiSn and HfNiSn synthesis attempts were carried out. The results obtained from these tests were also unsuccessful. Therefore, samples were prepared by making slight modifications to the methods previously mentioned. TiNiSn was prepared using three different approaches, termed (a), (b), and (c). In all three approaches, powders were combined and homogenized with a mortar and pestle, followed by cold pressing for approximately 20 minutes, and arc melting the pellets twice (once on each side). All methods involved annealing at 1073 K for one week. For method (a), the melted ingot was crushed with a mortar and pestle and annealed as a powder. In method (b) the ingot was crushed into a powder, homogenized with a mortar and pestle, cold pressed, and then annealed. Method (c) was the same as (b), however, the second pellet was arc melted twice (once on each side) and then annealed as an ingot. Side products were observed in all PXRD diagrams (Figure 22). However, only Ni_2TiSn was observed as a side product when examining the PXRD for the sample prepared by method (b). In addition, the amount of this side product was significantly less when compared to the other methods. R. A. Downie *et al.* and L. Chen *et al.* used similar approaches as they also annealed pelletized samples for preparing their HH materials.[18, 58]
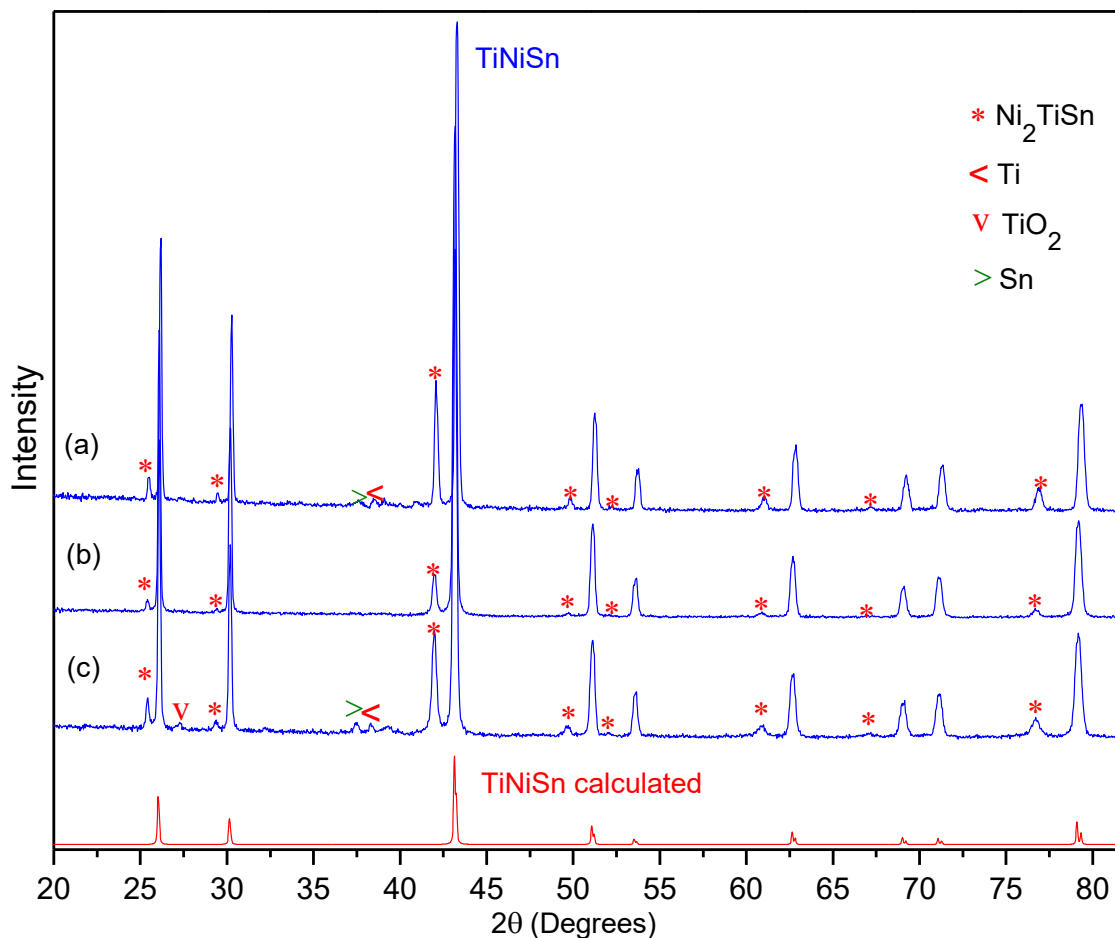
Figure 22: PXRD of TiNiSn for Methods (a), (b), and (c)

These approaches used for making TiNiSn were also applied for HfNiSn synthesis to see if method (b) is effective for synthesizing various HH materials. Method (a) was not attempted due to sample loss. This was a consequence of adhesive forces between the powder and the silica tube after annealing. The PXRD patterns for the HfNiSn samples (Figure 23) also indicate that method (b) is more effective for HH synthesis. With this method, fewer and less intense side product peaks are observed.
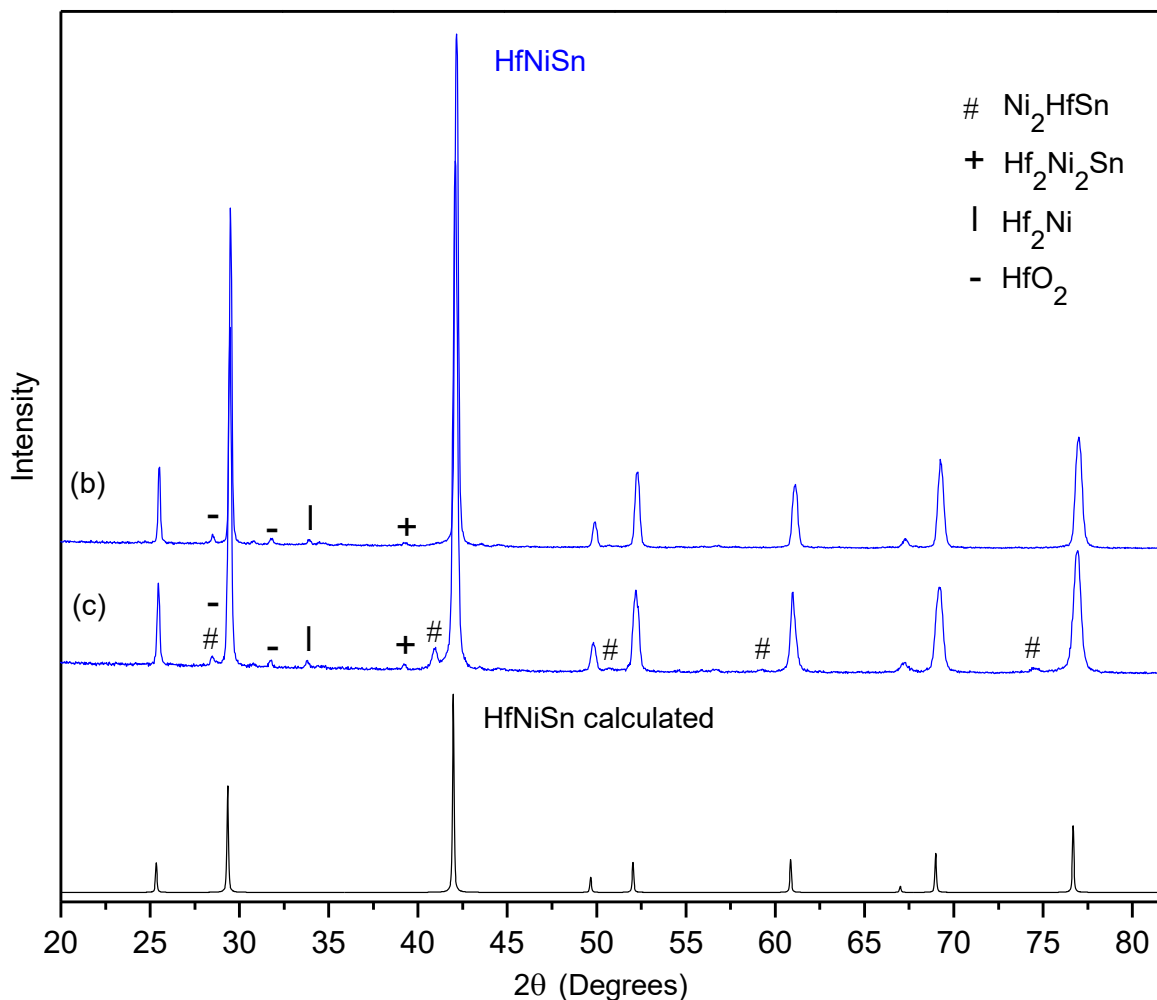
Figure 23: PXRD of HfNiSn for Methods (b) and (c)

To see if method (b) works on a large scale, bulk samples of TiNiSn and HfNiSn were prepared. Ni_2TiSn was present in the PXRD pattern after one week of annealing at 800°C (Figure 24a). The intensity of this side product was reduced by annealing at 1073 K for 2 weeks (Figure 24b). Annealing at 1173 K for 2 weeks resulted in a pure powder diagram of TiNiSn (Figure 24c). R. A. Downie *et al*. also used the same annealing temperature and duration for preparing HH compounds.[58] High purity HfNiSn PXRD diagrams were obtained after one week of

annealing at 1073 K. However, low intensity HfO_2 side product peaks were still present in the powder diagrams.
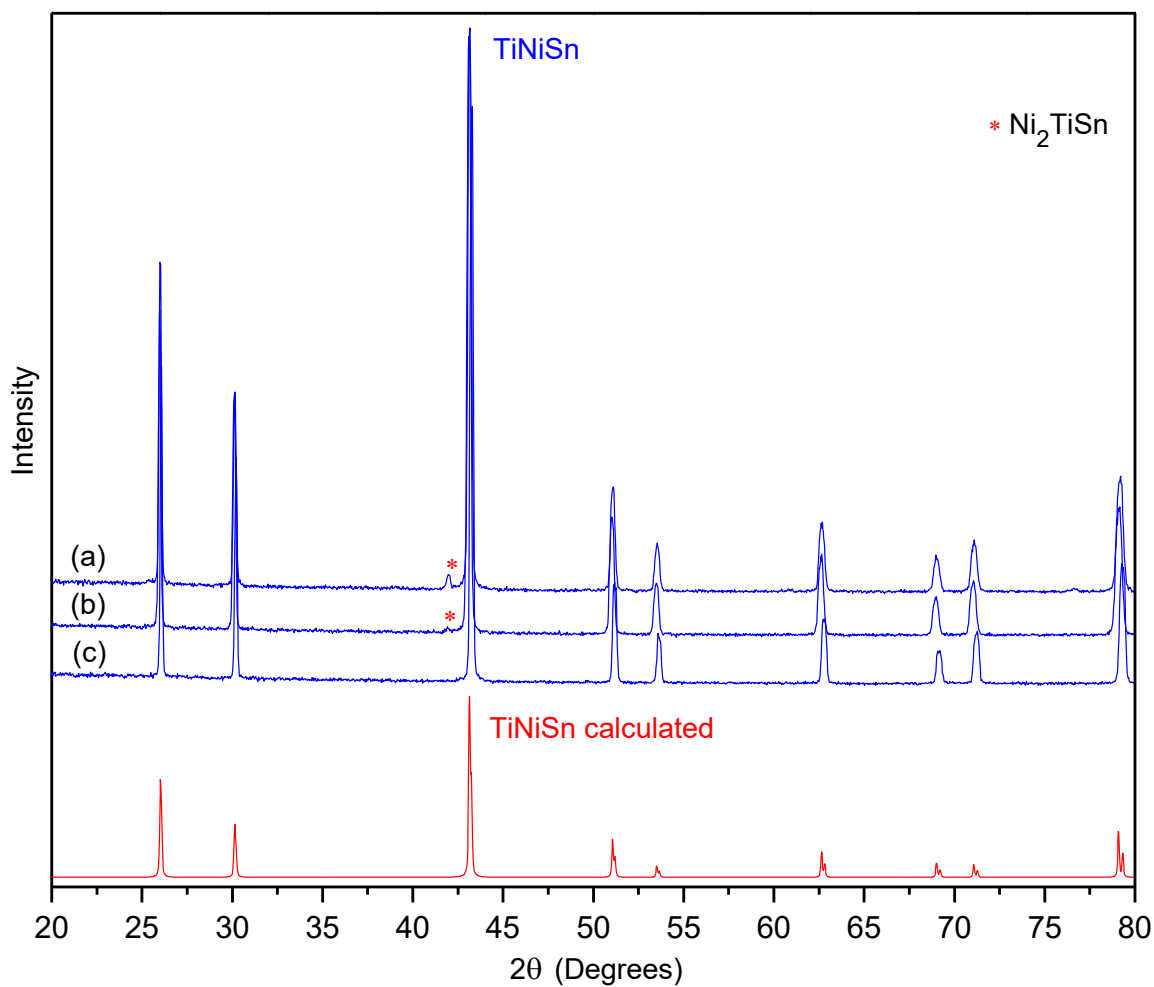
Figure 24: PXRD Diagrams for 1 gram TiNiSn samples annealed at (a) 1073 K for 1 week (b) 1073 K for 2 weeks (c) 1173 K for 2 weeks

4.1.4 $Ti_{0.5}Hf_{0.5}NiSn$, $Ti_{0.5}Zr_{0.25}Hf_{0.25}NiSn_{1-x}Sb_x$ and $Ti_{0.5}Zr_{0.25}Hf_{0.25}Co_xNi_{1-x}Sn$ Synthesis

$Ti_{0.5}Hf_{0.5}NiSn$ was synthesised using method (b) with two weeks of annealing at 1173 K.

However, Ni_2TiSn was observed as a side product in PXRD plots. This side product was

eliminated when annealing at 1173 K for three weeks (Figure 25a). This process was repeated for

all $Ti_{0.5}Zr_{0.25}Hf_{0.25}NiSn_{1-x}Sb_x$ and $Ti_{0.5}Zr_{0.25}Hf_{0.25}Co_xNi_{1-x}Sn$ samples. Other than HfO_2, no side

products were detected upon PXRD analysis. Undoped $Ti_{0.5}Zr_{0.25}Hf_{0.25}NiSn$, *n*-type

$Ti_{0.5}Zr_{0.25}Hf_{0.25}NiSn_{0.99}Sb_{0.01}$, and *p*-type $Ti_{0.5}Zr_{0.25}Hf_{0.25}Co_{0.20}Ni_{0.80}Sn$ PXRD diagrams are

displayed in Figures 25b, 25c, and 25d respectively.
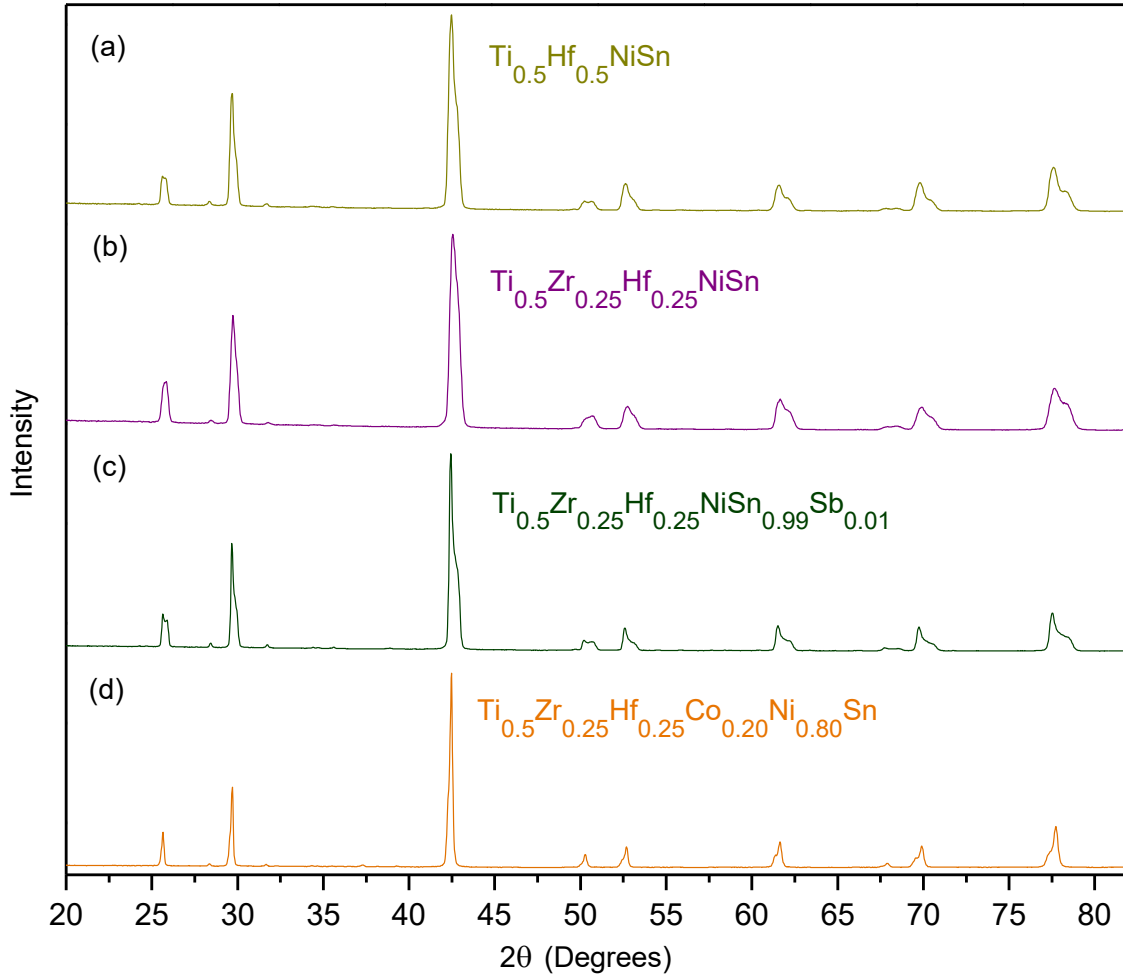
Figure 25: PXRD Diagrams of (a) $Ti_{0.5}Hf_{0.5}NiSn$ (b) $Ti_{0.5}Zr_{0.25}Hf_{0.25}NiSn$ (c) $Ti_{0.5}Zr_{0.25}Hf_{0.25}NiSn_{0.99}Sb_{0.01}$ (d) $Ti_{0.5}Zr_{0.25}Hf_{0.25}Co_{0.20}Ni_{0.80}Sn$
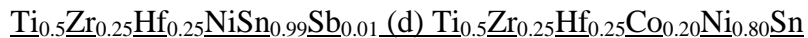
4.2 SEM-EDX

Scanning electron microscopy in conjunction with energy dispersive x-ray spectroscopy was performed on the *p*-type and *n*-type samples synthesized with the highest dopant concentration. The purpose of these experiments was to verify that the correct stoichiometry was maintained when synthesizing the HH materials.

SEM images of *p*-type $Ti_{0.5}Zr_{0.25}Hf_{0.25}Co_{0.20}Ni_{0.80}Sn$ in both powder form and pellet form are provided in Figures 26a and 26b respectively. In order, atomic percentages of 16.7 %, 7.9 %, 7.5 %, 8.10 %, 29.4 %, and 30.4 % were acquired for Ti, Zr, Hf, Co, Ni, and Sn from EDX spectroscopy analysis of the sample in powder form. For the pelletized sample, the atomic percentages are 16.9 %, 9.5 %, 9.1 %, 6.6 %, 25.0 %, and 33.0 % for Ti, Zr, Hf, Co, Ni, and Sn correspondingly. These values are relatively close to the expected values. When compared, all values differ by no more than 3 atomic percent. The expected values are 16.7 % for Ti, 8.3 % for Zr, 8.3 % for Hf, 6.7 % for Co, 26.7 % for Ni, and 33.3 % for Sn.
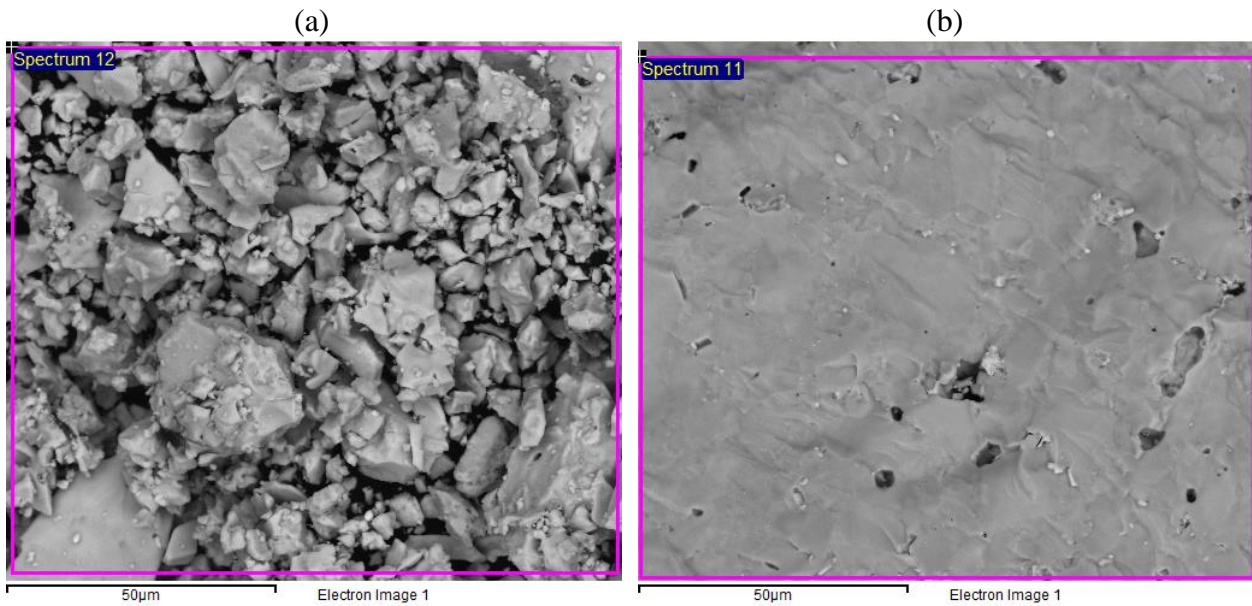
Figure 26: SEM Images of $Ti_{0.5}Zr_{0.25}Hf_{0.25}Co_{0.20}Ni_{0.80}Sn$ in (a) Powder Form (b) Pellet Form

SEM-EDX experiments were also conducted on *n*-type $Ti_{0.5}Zr_{0.25}Hf_{0.25}NiSn_{0.95}Sb_{0.05}$. SEM images were gathered for the sample in powder form (Figure 27a) and pellet form (Figure 27b). EDX analysis provided the following atomic percentages for the sample in powder form:

15.8 % for Ti, 8.0 % for Zr, 9.2 % for Hf, 34.7 % for Ni, 29.5 % for Sn, and 2.8 % for Sb. For

the pelletize sample, the atomic percentages are 16.8 %, 6.9 % 7.0 %, 34.5 %, 31.5 %, 3.3 % for

Ti, Zr, Hf, Ni, Sn and Sb respectively. These values closely match the expected values. The

measured atomic percentages for each element are less than 2.5 atomic percent different than the

expected values. In order, the expected atomic percentages for $Ti_{0.5}Zr_{0.25}Hf_{0.25}NiSn_{0.95}Sb_{0.05}$ are

16.7 %, 8.3 %, 8.3 %, 33.3 %, 31.7 %, and 1.7 % for titanium, zirconium, hafnium, nickel, tin

and antimony. Based on the SEM images in Figure 27a and 28a, the grain size of these HH
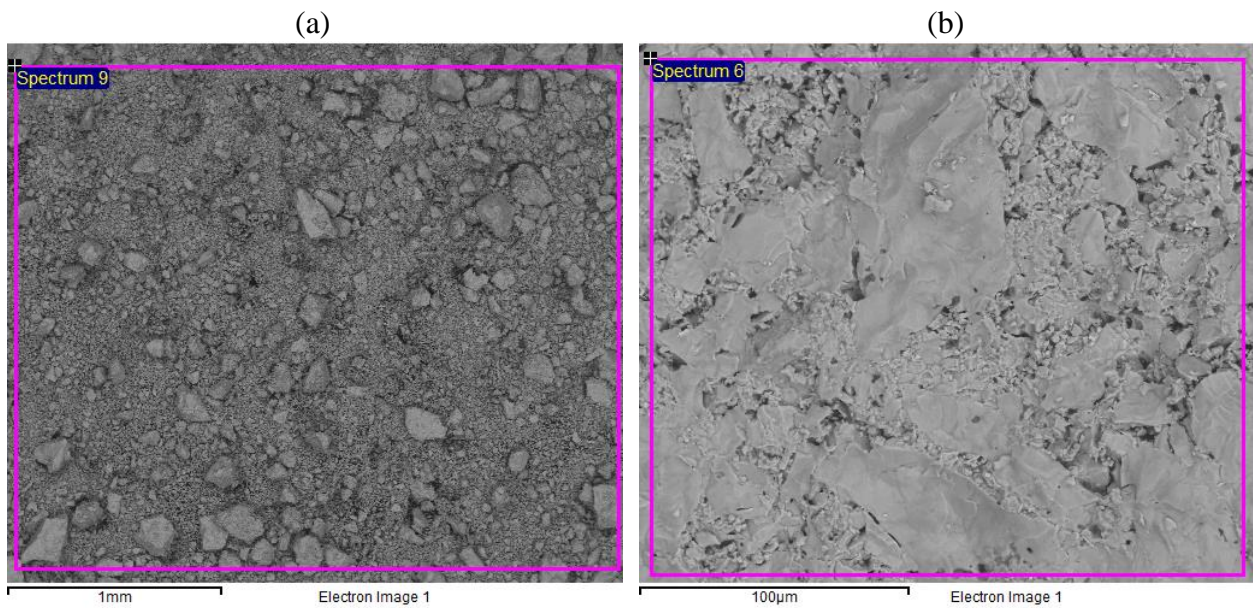
materials typically varies from 10 – 250 μm.

(a) (b)

Figure 27: SEM Images of $Ti_{0.5}Zr_{0.25}Hf_{0.25}NiSn_{0.95}Sb_{0.05}$ in (a) Powder Form (b) Pellet Form

4.3 Physical Properties

4.3.1 Undoped *M*NiSn Properties

TiNiSn and HfNiSn pellets used for physical property analysis were formed by hot-pressing samples at 1173 K for 1 hour. Using Equation (16), densities of 6.87 gcm^{-3} and 8.77gcm^{-3} were obtained for TiNiSn and HfNiSn respectively. These values are 96 % (TiNiSn) and 84 % (HfNiSn) of their respective theoretical density values.[60-61] Both percent densities are larger than the densities obtained by R.A. Downie *et al*. (77 % and 73 %) for TiNiSn and HfNiSn respectively.[58] In an attempt to improve sample density, Ti$_{0.5}$Hf$_{0.5}$NiSn and Ti$_{0.5}$Zr$_{0.25}$Hf$_{0.25}$NiSn samples were hot pressed at 1273 K for 2 hours. A high density of 7.94 gcm^{-3} (97 %) was obtained for Ti$_{0.5}$Hf$_{0.5}$NiSn. This is significantly higher than the 72 % density obtained by R.A. Downie *et al*.[58] However, the density obtained for Ti$_{0.5}$Zr$_{0.25}$Hf$_{0.25}$NiSn was only 7.30 gcm^{-3}; 89 % of the theoretical value.[19] The experimental, theoretical and percent densities of all undoped *M*NiSn (M = Ti, Zr, Hf) samples are summarized in Table 3.

Table 3: *M*NiSn Densities

Sample	Experimental Density (gcm^{-3})	Theoretical Density (gcm^{-3})	Percent Density (%)
TiNiSn	6.87	7.19[60]	96
HfNiSn	8.77	10.5[61]	84
Ti$_{0.5}$Hf$_{0.5}$NiSn	7.94	8.20[58]	97
Ti$_{0.5}$Zr$_{0.25}$Hf$_{0.25}$NiSn	7.30	8.21[19]	89

Physical property measurements were conducted from 330 – 900 K. All undoped materials show increasing electrical conductivity with increasing temperature throughout the entire temperature range. This matches the trend typically observed for intrinsic semiconductors. TiNiSn displays the highest σ at all temperatures. The σ of TiNiSn increased from 5.22 Ω^{-1}cm^{-1} at 330 K to 945 Ω^{-1}cm^{-1} at 900 K. In order, HfNiSn, Ti$_{0.5}$Hf$_{0.5}$NiSn, and Ti$_{0.5}$Zr$_{0.25}$Hf$_{0.25}$NiSn display electrical conductivities of 167 Ω^{-1}cm^{-1}, 189 Ω^{-1}cm^{-1}, and 204 Ω^{-1}cm^{-1} at 330 K. However, σ increases at a faster rate for HfNiSn when compared to the substituted materials. As a result, HfNiSn shows the highest σ = 696 Ω^{-1}cm^{-1} at 900 K. At this temperature, σ = 617 Ω^{-1}cm^{-1} for Ti$_{0.5}$Hf$_{0.5}$NiSn and 639 Ω^{-1}cm^{-1} for Ti$_{0.5}$Zr$_{0.25}$Hf$_{0.25}$NiSn. The electrical properties of the undoped MNiSn compounds mentioned above are shown in Figure 28a. By partially substituting the M site of TiNiSn with Zr and/or Hf, the number of defects increases. This causes relaxation time to decrease, resulting in lower mobility. As shown in equation (9), μ is related to electrical conductivity. Therefore, Ti$_{0.5}$Hf$_{0.5}$NiSn and Ti$_{0.5}$Zr$_{0.25}$Hf$_{0.25}$NiSn display lower σ when compared to TiNiSn. The low σ of HfNiSn in comparison to TiNiSn may be attributed to lower sample density resulting in lower mobility.
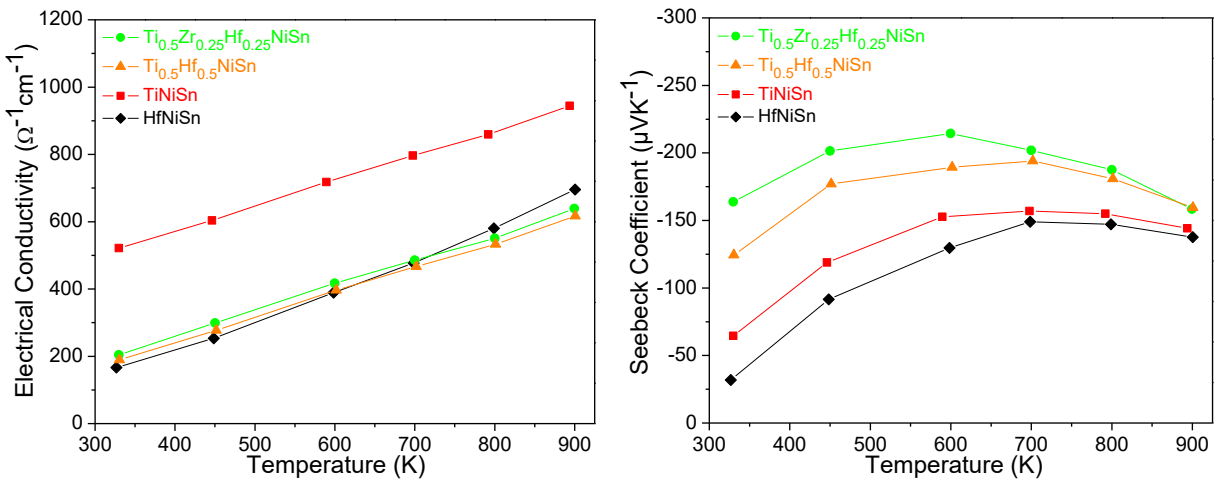

Figure 28: MNiSn (a) Electrical Conductivity (b) Seebeck Coefficient

52

All undoped MNiSn samples display a negative Seebeck coefficient from 330 K and 900 K, indicating n-type conduction. At low temperatures, S increases in the negative direction with increasing temperature. However, the opposite begins to occur somewhere between 550 and 750 K due to the bipolar effect. Overall $Ti_{0.5}Zr_{0.25}Hf_{0.25}NiSn$ shows the highest S, followed by $Ti_{0.5}Hf_{0.5}NiSn$, TiNiSn, and HfNiSn. For $Ti_{0.5}Zr_{0.25}Hf_{0.25}NiSn$, S = -164 at 330 K and increases to a maximum value of -214 μVK^{-1} at 600K. $Ti_{0.5}Hf_{0.5}NiSn$ at 330 K produces S = -124 μVK^{-1}, and displays its maximum Seebeck coefficient of -194 μVK^{-1} at 700 K. For TiNiSn, S ranges from -65 μVK^{-1} (330 K) to -157 μVK^{-1} (700 K). The Seebeck coefficient of HfNiSn ranges from -32 μVK^{-1} to -149 μVK^{-1} (700K) throughout the temperature range. Thermopower vs. temperature is illustrated in Figure 28b for all the undoped MNiSn materials described above.

The power factor of the undoped MNiSn samples from 330 – 900 K is displayed in Figure 29a. Since HfNiSn exhibits the lowest σ and S throughout the range, PF is also the lowest. The power factor of HfNiSn ranges from 0.17 – 13 $\mu W\ cm^{-1}K^{-2}$. Although TiNiSn displays the largest σ at 330 K, S is comparative large for $Ti_{0.5}Hf_{0.5}NiSn$. As a result, these two compounds produce nearly identical PF's at this temperature (2 $\mu W\ cm^{-1}K^{-2}$ for TiNiSn and 3 $\mu W\ cm^{-1}K^{-2}$ for $Ti_{0.5}Hf_{0.5}NiSn$). The largest PF at 330 K is 5 $\mu W\ cm^{-1}K^{-2}$, and it is observed in $Ti_{0.5}Zr_{0.25}Hf_{0.25}NiSn$ due to its significantly large S at this temperature. At 700 K, $Ti_{0.5}Zr_{0.25}Hf_{0.25}NiSn$ and $Ti_{0.5}Hf_{0.5}NiSn$ produce maximum power factor (PF_{max}) values of 20 $\mu W\ cm^{-1}K^{-2}$ and 18 $\mu W\ cm^{-1}K^{-2}$ respectively. However, TiNiSn exhibits a PF_{max} at 800 K since the decrease in S is minimal after 700 K. Due to high σ, TiNiSn produces the highest PF_{max} = 21 $\mu W\ cm^{-1}K^{-2}$ at 800 K for the undoped MNiSn materials.
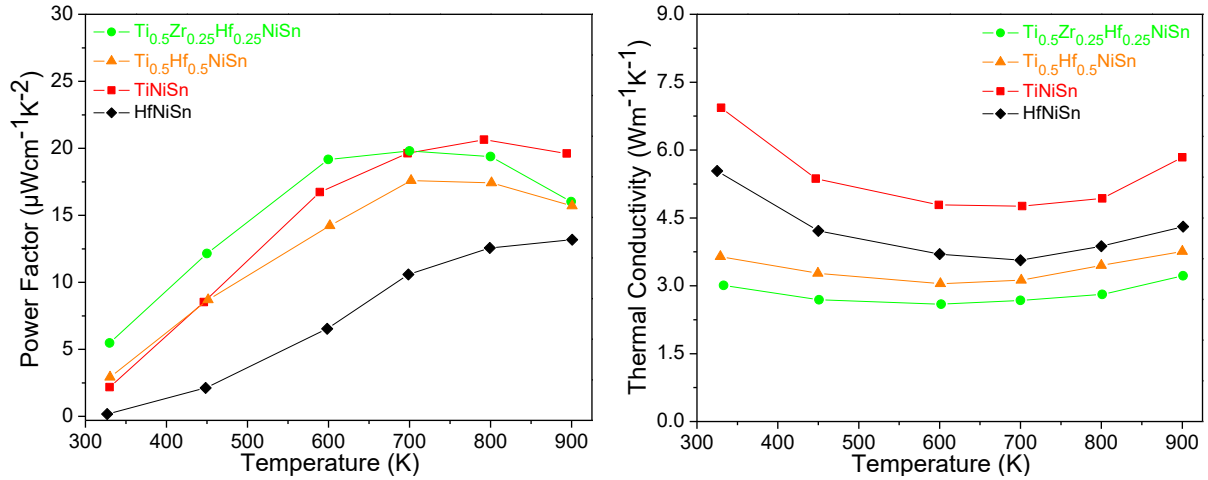
Figure 29: *M*NiSn (a) Power Factor (b) Total Thermal Conductivity

From 330 K to 900 K, the total thermal conductivity order from highest to lowest for the undoped *M*NiSn samples is TiNiSn, HfNiSn, $Ti_{0.5}Hf_{0.5}NiSn$, $Ti_{0.5}Zr_{0.25}Hf_{0.25}NiSn$. Throughout the temperature range, κ ranges from 4.76 W $m^{-1}K^{-1}$ - 6.93 W $m^{-1}K^{-1}$ for TiNiSn. This material exhibits the largest κ due to its high electrical and lattice contributions that range from 0.36 – 1.47 W $m^{-1}K^{-1}$ and 3.77 - 6.56 W $m^{-1}K^{-1}$ respectively. By replacing the M site with Hf, total thermal conductivity decreases. Throughout the temperature range, κ for HfNiSn ranges from 3.56 - 5.54 W $m^{-1}K^{-1}$. This decrease is mainly attributed to the decrease in κ_l. Lattice vibrations occur at lower frequencies when heavier elements are involved in the matrix.[35] For HfNiSn, κ_e and κ_l range from 0.13 – 1.10 W $m^{-1}K^{-1}$ and 2.99 – 5.41 W $m^{-1}K^{-1}$ respectively. Total thermal conductivity is lower in $Ti_{0.5}Hf_{0.5}NiSn$ and $Ti_{0.5}Zr_{0.25}Hf_{0.25}NiSn$ due to reductions in κ_l from mass fluctuation. For $Ti_{0.5}Hf_{0.5}NiSn$ κ, κ_e, and κ_l range from 3.05 – 3.76 W $m^{-1}K^{-1}$, 0.11 – 0.94 W $m^{-1}K^{-1}$, and 2.59 – 3.53 W $m^{-1}K^{-1}$ respectively. In order κ, κ_e, and κ_l range from 2.59 – 3.22 W $m^{-1}K^{-1}$, 0.11 – 0.98 W $m^{-1}K^{-1}$ and 2.08 – 2.89 W $m^{-1}K^{-1}$ for $Ti_{0.5}Zr_{0.25}Hf_{0.25}NiSn$. Physical property plots for κ, κ_e, and κ_l are displayed in Figures 29b, 30a and 30b respectively.
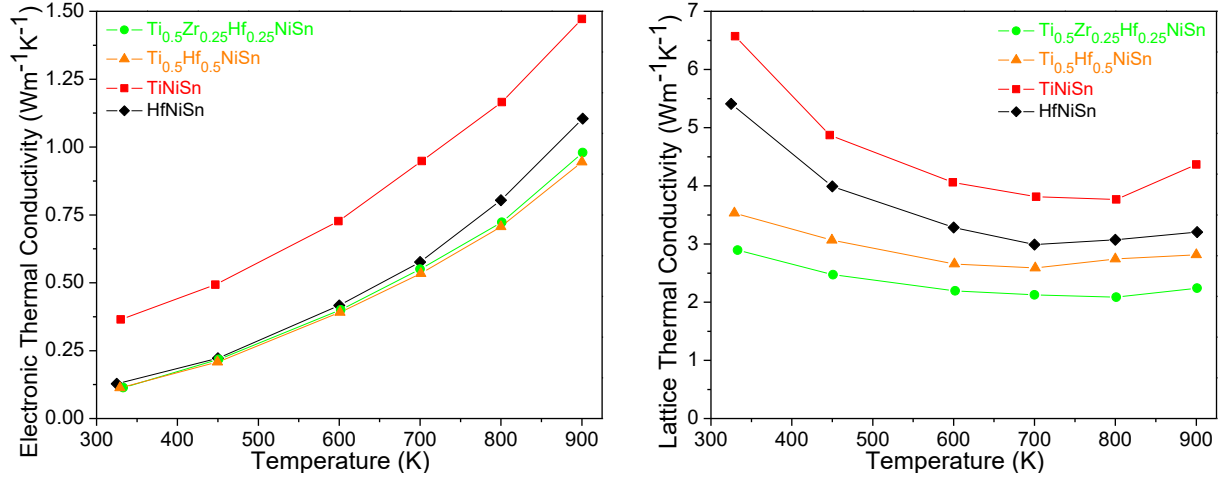
Figure 30: MNiSn (a) Electronic Contribution to Thermal Conductivity (b) Lattice Contribution

to Thermal Conductivity

To reiterate, HfNiSn displays the lowest PF as well as high κ when compared to the other

MNiSn samples. As a result, this compound produces the lowest figure of merit from 330 K –

900 K with a maximum figure of merit (ZT_{max}) of 0.28 at 900 K. Although TiNiSn displays the

highest PF at 800 K, it also exhibits the highest κ at this temperature. As a result, TiNiSn has the

second lowest ZT_{max} = 0.33 at 800 K. $Ti_{0.5}Hf_{0.5}NiSn$ has a low PF and κ when compared to

TiNiSn. The lower κ plays a more significant impact on the figure of merit, as $Ti_{0.5}Hf_{0.5}NiSn$

produces a ZT_{max} = 0.40 at 800 K. Due to a significantly large S and low κ_l, $Ti_{0.5}Zr_{0.25}Hf_{0.25}NiSn$

has a high PF and low κ when compared to the other MNiSn materials. Therefore, the figure of

merit of $Ti_{0.5}Zr_{0.25}Hf_{0.25}NiSn$ is highest from 330 – 900 K, with a ZT_{max} = 0.55 at 800 K. The

figure of merit vs. temperature is displayed for all MNiSn samples in Figure 31. The optimum

physical properties for the MNiSn samples are summarized in Table 4.
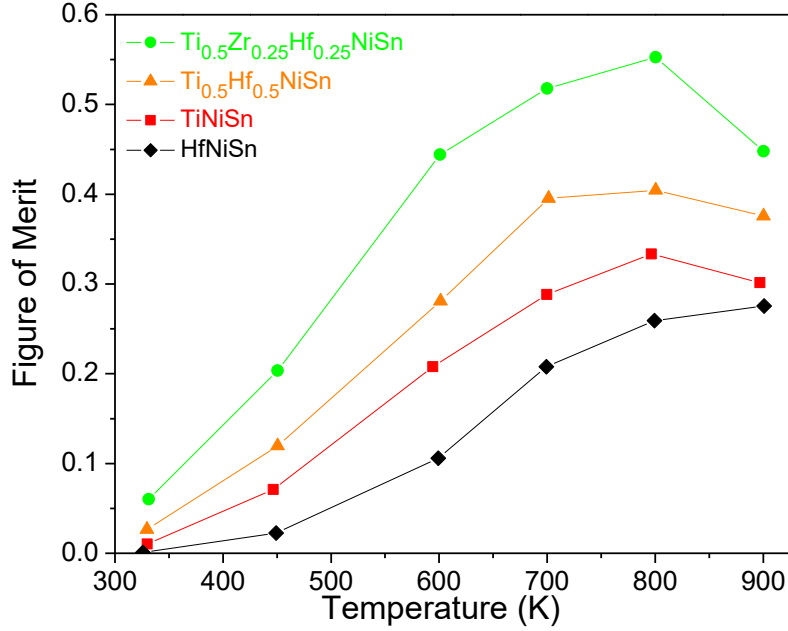
Figure 31: MNiSn Figure of Merit

Table 4: MNiSn Physical Properties at ZT_{max}

Sample	σ ($\Omega^{-1}cm^{-1}$)	S (μVK^{-1})	κ ($W\ m^{-1}K^{-1}$)	T (K)	ZT_{max}
TiNiSn	860	-155	4.93	800	0.33
HfNiSn	696	-138	4.31	900	0.28
$Ti_{0.5}Hf_{0.5}NiSn$	533	-181	3.45	800	0.40
$Ti_{0.5}Zr_{0.25}Hf_{02.5}NiSn$	551	-188	2.81	800	0.55

4.3.2 $Ti_{0.5}Zr_{0.25}Hf_{0.25}Co_xNi_{1-x}Sn$ Properties

$Ti_{0.5}Zr_{0.25}Hf_{0.25}Co_xNi_{1-x}Sn$ samples were pelletized by hot-pressing at 1273K for 2hr to

conduct physical property analysis. Unit cell refinement was performed on

$Ti_{0.5}Zr_{0.25}Hf_{0.25}Co_{0.03}Ni_{0.97}Sn$ and $Ti_{0.5}Zr_{0.25}Hf_{0.25}Co_{0.08}Ni_{0.92}Sn$ to obtain theoretical density.

These measurements were performed with the program known as "GSAS". Lattice parameters of

6.0041(4) Å and 6.0040(3) Å were obtained for these samples respectively. Both values compute to a theoretical density of 8.25 gcm^{-3}. $Ti_{0.5}Zr_{0.25}Hf_{0.25}Co_xNi_{1-x}Sn$ densities are shown in Table 5.

Table 5: $Ti_{0.5}Zr_{0.25}Hf_{0.25}Co_xNi_{1-x}Sn$ Densities

Sample	Experimental Density (gcm^{-3})	Theoretical Density (gcm^{-3})	Percent Density (%)
$Ti_{0.5}Zr_{0.25}Hf_{0.25}Co_{0.01}Ni_{0.99}Sn$	7.34	8.25	89
$Ti_{0.5}Zr_{0.25}Hf_{0.25}Co_{0.02}Ni_{0.98}Sn$	7.16	8.25	87
$Ti_{0.5}Zr_{0.25}Hf_{0.25}Co_{0.03}Ni_{0.97}Sn$	7.32	8.25	89
$Ti_{0.5}Zr_{0.25}Hf_{0.25}Co_{0.04}Ni_{0.96}Sn$	7.50	8.25	91
$Ti_{0.5}Zr_{0.25}Hf_{0.25}Co_{0.05}Ni_{0.95}Sn$	7.26	8.25	88
$Ti_{0.5}Zr_{0.25}Hf_{0.25}Co_{0.08}Ni_{0.92}Sn$	7.49	8.25	91
$Ti_{0.5}Zr_{0.25}Hf_{0.25}Co_{0.15}Ni_{0.85}Sn$	7.74	8.25	94
$Ti_{0.5}Zr_{0.25}Hf_{0.25}Co_{0.20}Ni_{0.80}Sn$	8.02	8.25	97

The electrical transport properties of all $Ti_{0.5}Zr_{0.25}Hf_{0.25}Co_xNi_{1-x}Sn$ samples ($0 \leq x \leq 0.20$) were measured from 330 – 900 K (Figure 32a). Throughout the entire temperature range, all samples display increasing σ with increasing temperature. At 330 K and 900 K, electrical conductivity varies from 82 – 218 $\Omega^{-1}cm^{-1}$ and 319 – 639 $\Omega^{-1}cm^{-1}$ respectively. At all temperatures, $Ti_{0.5}Zr_{0.25}Hf_{0.25}Co_xNi_{1-x}Sn$ shows decreasing σ with increasing cobalt concentration when x falls within the following regions: $0 \leq x \leq 0.02$, $0.04 \leq x \leq 0.05$ and $0.08 \leq x \leq 0.15$. The opposite occurs when the Co content ranges from $0.03 \leq x \leq 0.04$, $0.05 \leq x \leq 0.08$, and $0.15 \leq x \leq 0.20$. The σ trend of $Ti_{0.5}Zr_{0.25}Hf_{0.25}Co_xNi_{1-x}Sn$ with respect to Co content does not match that

observed in Bi_2Te_3 with varying Te content (Figure 6). A plausible explanation as to why this occurred has yet to be determined.
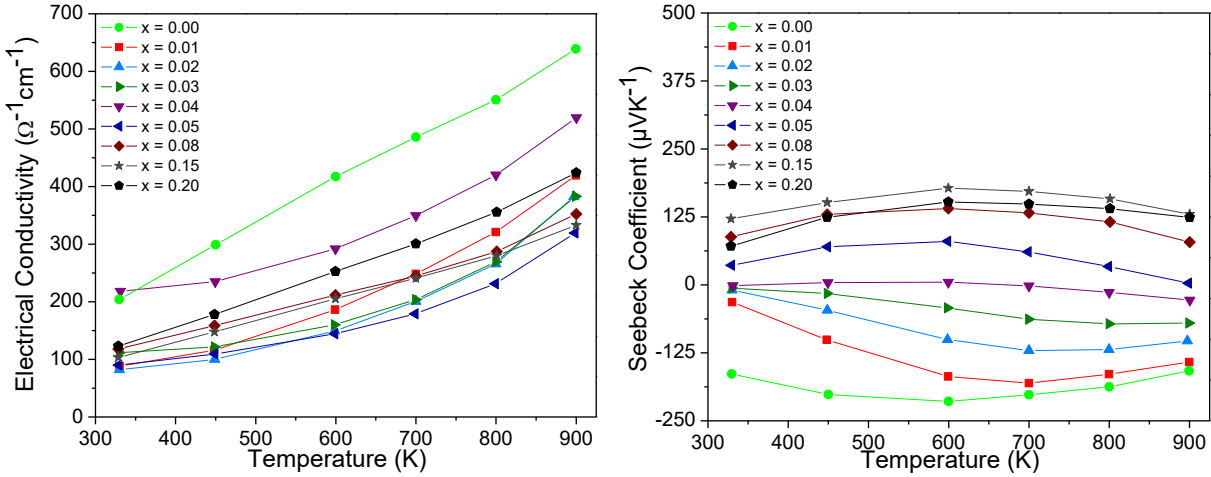
Figure 32: $Ti_{0.5}Zr_{0.25}Hf_{0.25}Co_xNi_{1-x}Sn$ (a) Electrical Conductivity (b) Seebeck Coefficient

From 330 – 900 K, the Seebeck coefficient of $Ti_{0.5}Zr_{0.25}Hf_{0.25}Co_xNi_{1-x}Sn$ increases in the positive direction with increasing x content until a maximum is produced at x = 0.15 (Figure 32b). The S trend with increasing Co content mimics that observed for Bi_2Te_3 with increasing Te content (Figure 6). A transition from negative to positive S was also observed by S. Katsuyama *et al*. when increasing the yttrium content of $Zr_{1-x}Y_xNiSn$.[50] When the cobalt content ranges from $0 \leq x \leq 0.03$, *n*-type conduction occurs as S is negative from 330 – 900 K. A transition point is observed when x = 0.04. At this concentration, S is positive S below 700 K and negative otherwise. When x $\geq$ 0.05, *p*-type conduction is observed as S is positive throughout the temperature range. At 330 K, S varies from -164 µV/K to 121 µV/K. The maximum Seebeck coefficient for $Ti_{0.5}Zr_{0.25}Hf_{0.25}Co_xNi_{1-x}Sn$ is typically produced around 600 K. At this temperature, S varies from -214 µV/K to 178 µV/K. Decreasing S with increasing temperature is

observed in all samples above 600 K due to the bipolar effect. At 900 K, the Seebeck coefficient of $Ti_{0.5}Zr_{0.25}Hf_{0.25}Co_xNi_{1-x}Sn$ samples falls within -158 µV/K to 130 µV/K.

From 330 – 900 K, the power factor of undoped $Ti_{0.5}Zr_{0.25}Hf_{0.25}NiSn$ is significantly larger than the Co doped samples. Throughout the temperature range, *PF* ranges from 5 – 20 µW $cm^{-1}K^{-2}$ for $Ti_{0.5}Zr_{0.25}Hf_{0.25}NiSn$. However, the power output of the cobalt doped samples is in the range of 0 – 7 µW $cm^{-1}K^{-2}$. This is due to a significantly smaller *S* and σ in $Ti_{0.5}Zr_{0.25}Hf_{0.25}Ni_{1-x}CoSn$ at all temperatures. Co doped samples show decreasing *PF* from $0 \leq x \leq 0.04$ and increasing *PF* from $0.04 \leq x \leq 0.15$. This is the same trend observed for *S*. Hence, the Seebeck coefficient of $Ti_{0.5}Zr_{0.25}Hf_{0.25}Co_xNi_{1-x}Sn$ materials plays a more significant factor than σ towards the power factor. *PF* is shown for all $Ti_{0.5}Zr_{0.25}Hf_{0.25}Co_xNi_{1-x}Sn$ samples as well as undoped $Ti_{0.5}Zr_{0.25}Hf_{0.25}NiSn$ in Figure 33a.
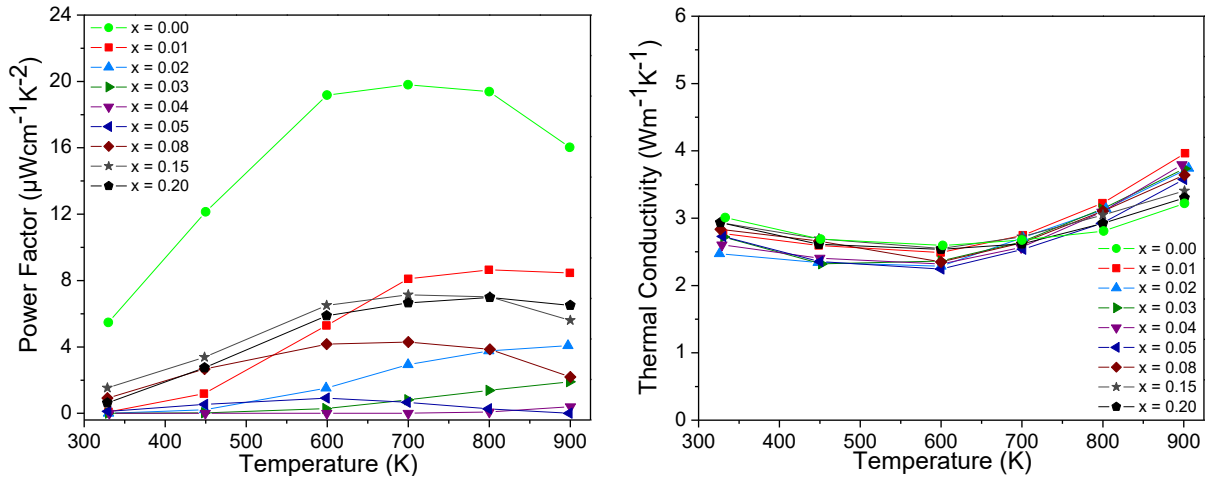
Figure 33: $Ti_{0.5}Zr_{0.25}Hf_{0.25}Co_xNi_{1-x}Sn$ (a) Power Factor (b) Total Thermal Conductivity

$Ti_{0.5}Zr_{0.25}Hf_{0.25}Co_xNi_{1-x}Sn$ ($0 \leq x \leq 0.20$) shows the same trends in total thermal conductivity and lattice thermal conductivity from 330 – 900 K. Thus, κ_l has a more significant

impact on κ than than κ_e. From 330 – 600 K, κ and κ_l decrease with increasing temperature. At 330 K, the Co doped samples show κ in the range of 2.47 – 3.01 W m^{-1}K^{-1} and κ_l in the range of 2.41 – 2.89 W m^{-1}K^{-1}. These materials produce lowest value of κ and κ_l at 600 K. These values vary from 2.24 – 2.59 W m^{-1}K^{-1} for κ and 1.89 – 2.35 W m^{-1}K^{-1} for κ_l. Above 600 K, both properties increase with increasing temperature due to the bipolar effect. In order, $Ti_{0.5}Zr_{0.25}Hf_{0.25}Co_xNi_{1-x}Sn$ produces κ and κ_l values that range from 3.22 – 3.96 W m^{-1}K^{-1} and 2.24 – 3.30 W m^{-1}K^{-1} at 900 K. From one dopant concentration to the next, κ values typically fall within error. However, a similar trend in κ with respect to Co content is observed at most temperatures. This pattern closely mimics that observed for Bi_2Te_3 with increasing Te content.

To restate, σ increases with increasing temperature from 330 – 900 K. A similar trend was observed for the electronic contribution to thermal conductivity (Figure 34a). Recall that κ_e increases when σ or temperature increases (Equation (10)). At 330 K and 900 K, $Ti_{0.5}Zr_{0.25}Hf_{0.25}Co_xNi_{1-x}Sn$ materials display κ_e values that fall within 0.06 – 0.18 W m^{-1}K^{-1} and 0.54 – 1.11 W m^{-1}K^{-1} respectively.
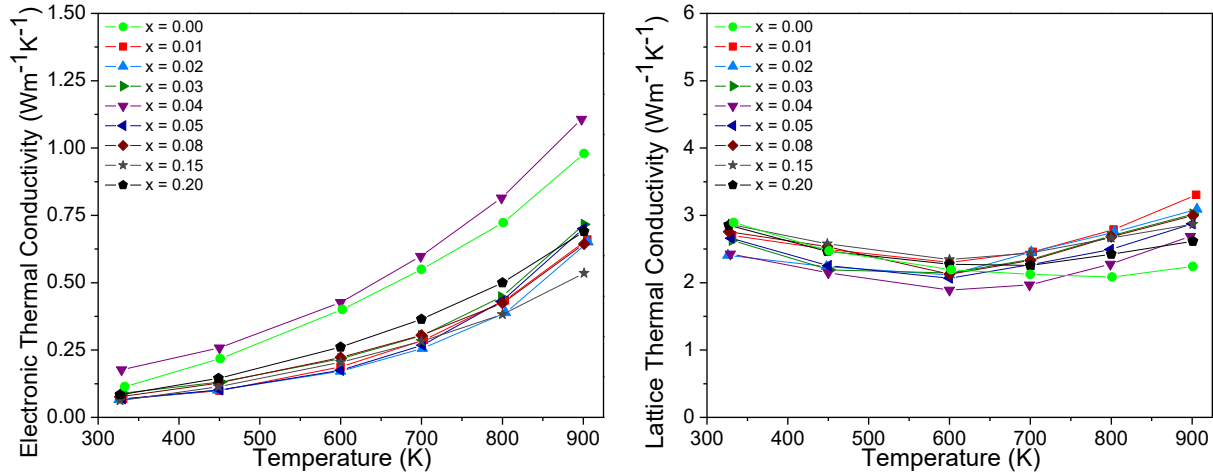
Figure 34: (a) $Ti_{0.5}Zr_{0.25}Hf_{0.25}Co_xNi_{1-x}Sn$ Electronic Contribution to Thermal Conductivity (b)

Lattice Contribution to Thermal Conductivity

Doping the nickel site of $Ti_{0.5}Zr_{0.25}Hf_{0.25}NiSn$ with cobalt causes substantial reductions to the figure of merit from 330 – 900 K (Figure 35). This is caused by significantly smaller S as well as lower σ. ZT varies from 0.06 – 0.55 for the undoped compound, and 0.001 – 0.21 for the Co doped samples from 330 – 900 K. On average, ZT decreases with increasing Co content when $0 \leq x \leq 0.04$. The opposite occurs when the Co concentration falls within $0.04 \leq x \leq 0.15$. The highest ZT_{max} for a $Ti_{0.5}Zr_{0.25}Hf_{0.25}Co_xNi_{1-x}Sn$ sample was 0.21. This was obtained with x = 0.01 at a temperature of 800 K. However, this material displays n-type conduction. For the samples that show p-type conduction (x > 0.04), the highest ZT_{max} was 0.19 at 800 K. This was achieved with a Co concentration of x = 0.20. However, this falls within error when compared to the ZT_{max} = 0.18 obtained for x = 0.15 at 800 K. These figures of merit are over 2.5 times smaller than the ZT_{max} obtained by X. Yan *et al*. for $Zr_{0.5}Hf_{0.5}CoSb_{0.8}Sn_{0.2}$ as an ingot.[20] In conclusion, Co is not an effective dopant for synthesizing p-type HH materials with large figures of merit. Based on these finding, no attempts were made on improving ZT by adding ZrO_2 nano-particles.
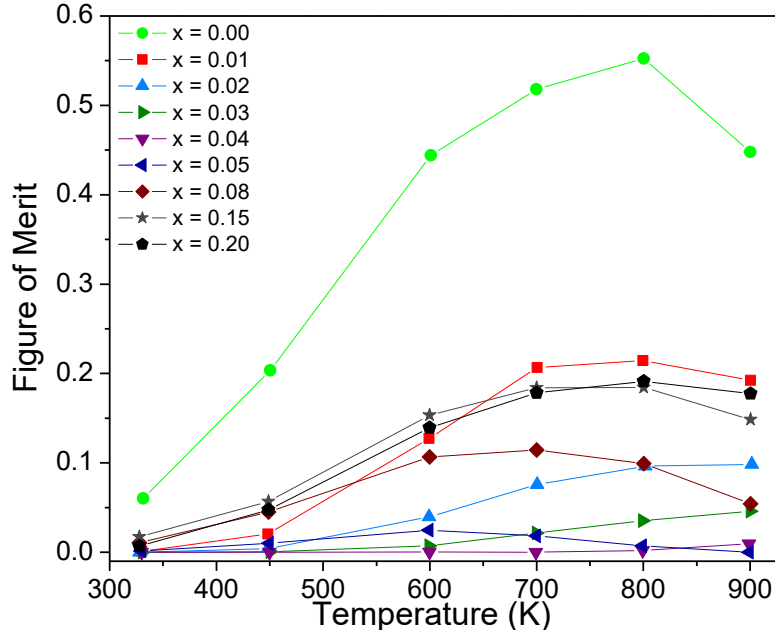
Figure 35: $Ti_{0.5}Zr_{0.25}Hf_{0.25}Co_xNi_{1-x}Sn$ Figure of Merit

Table 6: $Ti_{0.5}Zr_{0.25}Hf_{0.25}Co_xNi_{1-x}Sn$ Physical Properties at ZT_{max}

Sample	σ ($\Omega^{-1}cm^{-1}$)	S (μVK^{-1})	κ (W m^{-1}K^{-1})	T (K)	ZT_{max}
$Ti_{0.5}Zr_{0.25}Hf_{0.25}NiSn$	551	-188	2.81	800	0.55
$Ti_{0.5}Zr_{0.25}Hf_{0.25}Co_{0.01}Ni_{0.99}Sn$	321	-164	3.22	800	0.21
$Ti_{0.5}Zr_{0.25}Hf_{0.25}Co_{0.02}Ni_{0.98}Sn$	382	-103	3.74	900	0.10
$Ti_{0.5}Zr_{0.25}Hf_{0.25}Co_{0.03}Ni_{0.97}Sn$	383	-70	3.74	900	0.05
$Ti_{0.5}Zr_{0.25}Hf_{0.25}Co_{0.04}Ni_{0.96}Sn$	520	-28	3.80	900	0.01
$Ti_{0.5}Zr_{0.25}Hf_{0.25}Co_{0.05}Ni_{0.95}Sn$	144	80	2.24	600	0.02
$Ti_{0.5}Zr_{0.25}Hf_{0.25}Co_{0.08}Ni_{0.92}Sn$	245	133	2.63	700	0.11
$Ti_{0.5}Zr_{0.25}Hf_{0.25}Co_{0.15}Ni_{0.85}Sn$	280	158	3.05	800	0.18
$Ti_{0.5}Zr_{0.25}Hf_{0.25}Co_{0.20}Ni_{0.80}Sn$	356	140	2.92	800	0.19

4.3.3 $Ti_{0.5}Zr_{0.25}Hf_{0.25}NiSn_{1-x}Sb_x$ Properties

All n-type doped $Ti_{0.5}Zr_{0.25}Hf_{0.25}NiSn_{1-x}Sb_x$ samples ($0.005 \leq x \leq 0.05$) were hot-pressed

for 2 hours at 1273 K for physical property measurements. The "GSAS" program was used to

perform unit cell refinement on three n-type samples. The lattice parameters obtained for

$Ti_{0.5}Zr_{0.25}Hf_{0.25}NiSn_{0.99}Sb_{0.01}$ and $Ti_{0.5}Zr_{0.25}Hf_{0.25}NiSn_{0.95}Sb_{0.05}$ were 6.0282(3) Å and 6.0274(3)

Å respectively.

Table 7: n-type doped $Ti_{0.5}Zr_{0.25}Hf_{0.25}NiSn_{1-x}Sb_x$ Densities

Sample	Experimental Density (gcm^{-3})	Theoretical Density (gcm^{-3})	Percent Density (%)
$Ti_{0.5}Zr_{0.25}Hf_{0.25}NiSn_{0.995}Sb_{0.005}$	7.43	8.16	91
$Ti_{0.5}Zr_{0.25}Hf_{0.25}NiSn_{0.99}Sb_{0.01}$	7.34	8.15	90
$Ti_{0.5}Zr_{0.25}Hf_{0.25}NiSn_{0.98}Sb_{0.02}$	7.33	8.16	90
$Ti_{0.5}Zr_{0.25}Hf_{0.25}NiSn_{0.97}Sb_{0.03}$	7.23	8.16	89
$Ti_{0.5}Zr_{0.25}Hf_{0.25}NiSn_{0.96}Sb_{0.04}$	7.45	8.16	91
$Ti_{0.5}Zr_{0.25}Hf_{0.25}NiSn_{0.95}Sb_{0.05}$	7.21	8.16	88

When x is between 0.005 and 0.02, $Ti_{0.5}Zr_{0.25}Hf_{0.25}NiSn_{1-x}Sb_x$ shows decreasing σ with

increasing temperature from 330 – 800 K. Electrical conductivity increases when heated from

800 – 900 K. This matches the trend that is typically observed for lightly doped extrinsic

semiconductors. When $x > 0.02$, σ decreases throughout the entire temperature range. This

matches the progression typically observed for heavily doped semiconductors. When a solid is

exposed to thermal energy, atoms within that material vibrate. The higher the energy, the faster

the atom vibrates. Since multiple atoms are held together by chemical bonds, multiple atoms oscillate together in a wavelike fashion when exposed to thermal energy. These lattice vibrations are referred to as phonons. Phonons can interact with electrons moving through the material, causing them to scatter. This results in decreased mobility, which is directly related to electrical conductivity (Equation (9)). This explains why a decrease in σ is observed with increasing temperature. For the lightly doped samples, the increase in σ above 800 K is due to the activation of intrinsic carriers from the valence band to the conductance band in significant numbers. As expected, σ increases with increasing carrier concentration (Equation (9)). Also, as n increases, σ decreases at a slower rate. At 300 K, σ ranges from 665 $\Omega^{-1}cm^{-1}$ (x = 0.005) to 3792 $\Omega^{-1}cm^{-1}$ (x = 0.05). At 900 K, a range of 678 $\Omega^{-1}cm^{-1}$ (x = 0.005) to 1823 $\Omega^{-1}cm^{-1}$ (x = 0.05) is observed for σ. Electrical conductivity for $Ti_{0.5}Zr_{0.25}Hf_{0.25}NiSn_{1-x}Sb_x$ (x = 0 to x = 0.05) is shown in Figure 36a from 330 K – 900 K.
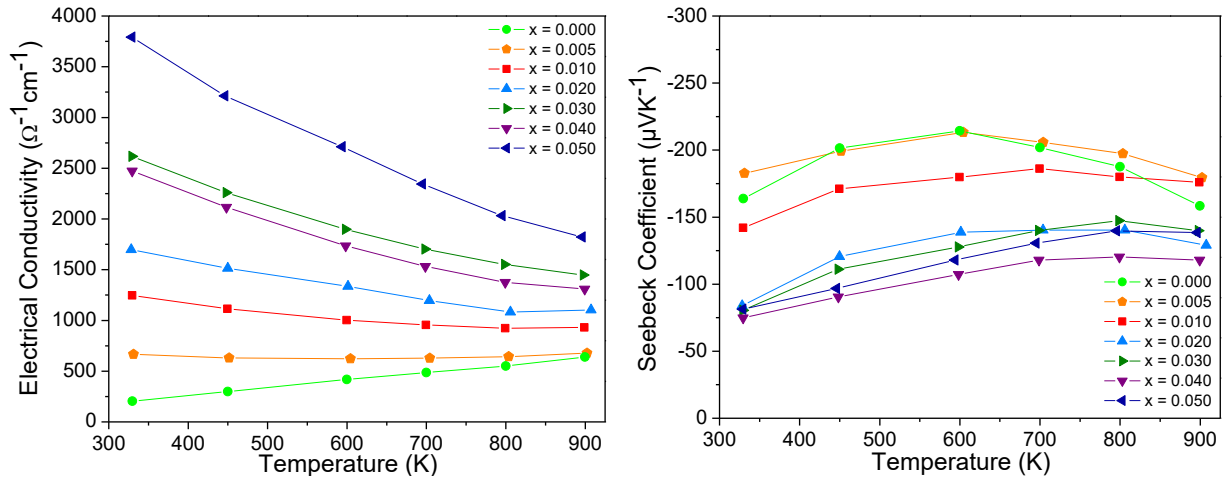

Figure 36: $Ti_{0.5}Zr_{0.25}Hf_{0.25}NiSn_{1-x}Sb_x$ (a) Electrical Conductivity (b) Seebeck Coefficient

As anticipated, all $Ti_{0.5}Zr_{0.25}Hf_{0.25}NiSn_{1-x}Sb_x$ samples exhibit a negative Seebeck coefficient from 330 K to 900 K, indicating n-type conduction. The Seebeck coefficient and

carrier concentration have an inverse relationship as shown in the Mott formula (Equation (8)).

This relationship is also observed in the S vs. temperature plots of the n-type doped samples

(Figure 36b). When x = 0.005, S = -183 μVK^{-1} at 300 K. S increases in the negative direction to -

213 μVK^{-1} at 600 K, and decreases to -179 μVK^{-1} at 900 K. At the highest n (x = 0.05), S = -81

μVK^{-1} at 300 K, and increases to a maximum of -140 μVK^{-1} at 800 K. After 800 K, S decreases

with temperature due to the bipolar effect. For x = 0.05, S = -138 μVK^{-1} at 900 K.

N. Shutoh and S. Sakurada also observed increasing S with increasing n. However, the

values of S differ significantly. For $Ti_{0.5}Zr_{0.25}Hf_{0.25}NiSn_{0.99}Sb_{0.01}$, N. Shutoh and S. Sakurada

obtained a maximum Seebeck coefficient (S_{max}) around -243 μVK^{-1} at 673 K. However, the S

results displayed in Figure 36b illustrates a S_{max} = -186 μVK^{-1} at 700 K. This results in a percent

difference of 23 %. N. Shutoh and S. Sakurada also reported a $S_{max} \approx$ -281 μVK^{-1} at 650 K when

x =0.006. When comparing this to the x =0.005 sample measured in this project, $S_{max} \approx$ -213

μVK^{-1} at 600 K. These two values differ by 24 %.

$Ti_{0.5}Zr_{0.25}Hf_{0.25}NiSn$ produces large Seebeck coefficients from 330 – 900 K when

compared to the antimony doped samples. However, σ is significantly lower for the undoped

material, resulting in lower power factors throughout the entire temperature range. At 330 K,

$Ti_{0.5}Zr_{0.25}Hf_{0.25}NiSn_{1-x}Sb_x$ (0 $\leq$ x $\leq$ 0.05) samples produce power factors that range from 5 – 25

$\mu W\ cm^{-1}K^{-2}$. When x = 0.01, PF = 25 $\mu W\ cm^{-1}K^{-2}$ at 330 K. This concentration displays the

highest PF at this temperature due to intermediate electrical and Seebeck properties of 1248 $\Omega^{-1}cm^{-1}$ and -142 μVK^{-1} respectively. $Ti_{0.5}Zr_{0.25}Hf_{0.25}NiSn_{0.95}Sb_{0.05}$ exhibits the highest PF above

600 K, with a PF_{max} = 40 $\mu W\ cm^{-1}K^{-2}$ at 700 K. This is due to high σ and an increasing S

throughout most of the temperature range. At 900 K, *n*-type samples display *PF*'s in the range of 16 - 35 µW cm^{-1}K^{-2} (Figure 37a)
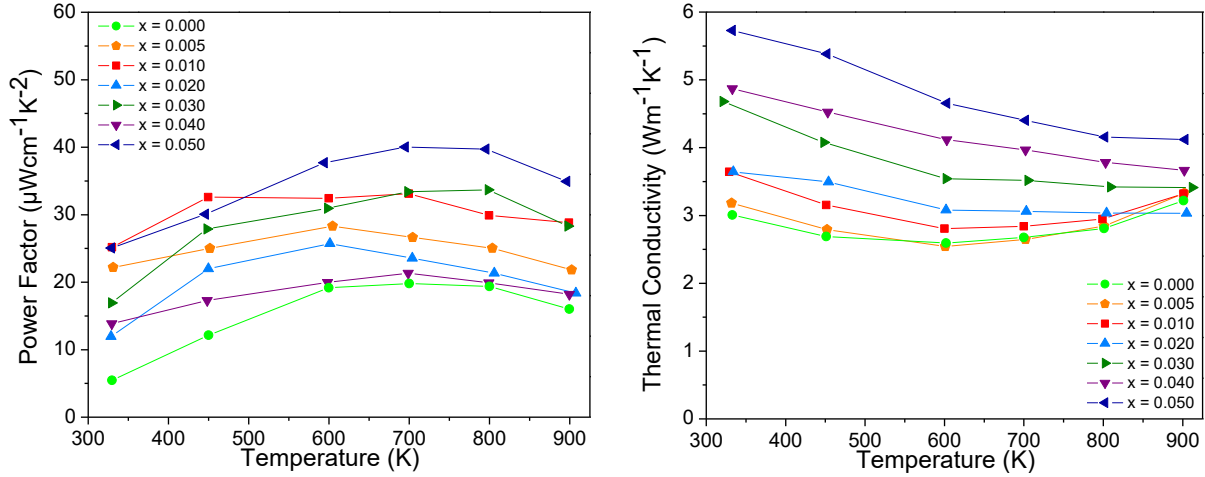

Figure 37: Ti$_{0.5}$Zr$_{0.25}$Hf$_{0.25}$NiSn$_{1-x}$Sb$_x$ (a) Power Factor (b) Total Thermal Conductivity

Total thermal conductivity and κ_e both increase with increasing carrier concentration for Ti$_{0.5}$Zr$_{0.25}$Hf$_{0.25}$NiSn$_{1-x}$Sb$_x$ (Figures 37b and 38a). These trends occur due to the relationships between κ_e, σ, and *n* (Equations (9) and (10)). At 330 K, κ ranges from 3.01 Wm^{-1}K^{-1} (x = 0) to 5.73 Wm^{-1}K^{-1} (x = 0.05). At this temperature, κ_e varies from 0.11 Wm^{-1}K^{-1} (x = 0) to 2.51 Wm^{-1}K^{-1} (x = 0.05). Samples with x $\geq$ 0.02 show a decreasing κ with increasing temperature. However, when x $\leq$ 0.01, an upturn in κ is observed around 600 K. This is due an increase in κ_l at this temperature, which is a product of the bipolar effect. This effect causes significant differences in κ_l at 900 K as shown in Figure 38b. As a result, Ti$_{0.5}$Zr$_{0.25}$Hf$_{0.25}$NiSn$_{0.98}$Sb$_{0.02}$ produces the lowest κ = 3.03 Wm^{-1}K^{-1} and 900 K due to a low κ_l = 1.24 Wm^{-1}K^{-1}. At 900 K κ, κ_e, and κ_l range from 3.03 – 4.12 Wm^{-1}K^{-1}, 0.98 – 2.88 Wm^{-1}K^{-1}, and 1.24 Wm^{-1}K^{-1} – 2.32 Wm^{-1}K^{-1} respectively.

N. Shutoh and S. Sakurada only display κ, and κ_l values at 293 K and 773 K for samples with $0 \le x \le 0.006$. For $Ti_{0.5}Zr_{0.25}Hf_{0.25}NiSn_{0.994}Sb_{0.006}$, $\kappa \approx 3.25$ $Wm^{-1}K^{-1}$ at 293 K and 2.86 $Wm^{-1}K^{-1}$ at 773 K. These values closely mimic the result obtained in this project for $Ti_{0.5}Zr_{0.25}Hf_{0.25}NiSn_{0.995}Sb_{0.005}$. At this composition, a $\kappa = 3.18$ $Wm^{-1}K^{-1}$ at 330 K and 2.84 $Wm^{-1}K^{-1}$ at 800 K was obtained. This calculates to a difference of 2 % at the lower temperatures and < 1% at the higher temperatures. However, the values obtained for κ_l shower larger differences. In order, the approximate κ_l values for $Ti_{0.5}Zr_{0.25}Hf_{0.25}NiSn_{0.994}Sb_{0.006}$ obtained by N. Shutoh and S. Sakurada at 293 K and 773 K are 1.85 $Wm^{-1}K^{-1}$ and 2.24 $Wm^{-1}K^{-1}$. The κ_l results obtained in this project for $Ti_{0.5}Zr_{0.25}Hf_{0.25}NiSn_{0.995}Sb_{0.005}$ are 2.82 $Wm^{-1}K^{-1}$ at 330 K (52 % difference) and 2.00 $Wm^{-1}K^{-1}$ at 800 K (11 % difference).
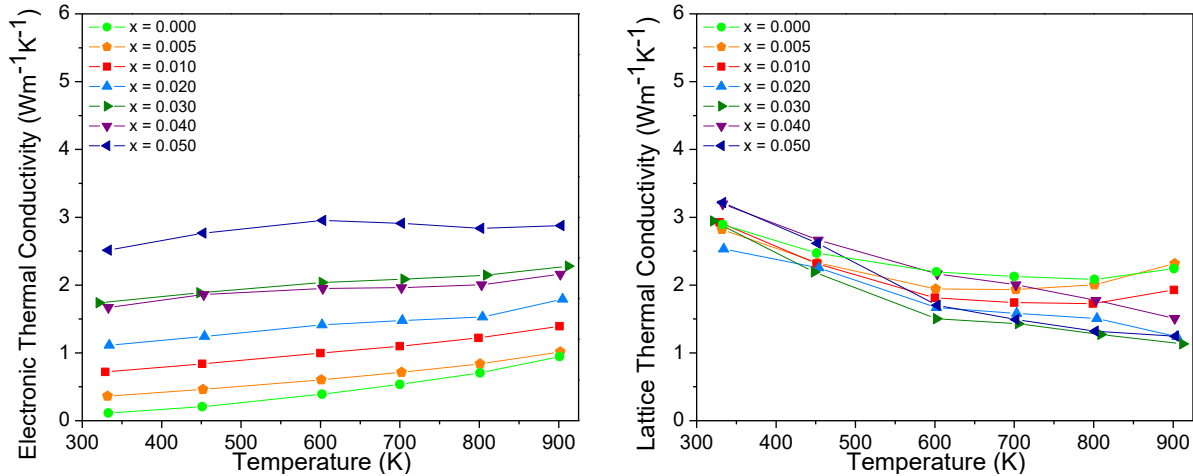
Figure 38: $Ti_{0.5}Zr_{0.25}Hf_{0.25}NiSn_{1-x}Sb_x$ (a) Electronic Contribution to Thermal Conductivity (b) Lattice Contribution to Thermal Conductivity

Doping the tin site of $Ti_{0.5}Zr_{0.25}Hf_{0.25}NiSn$ with small amounts of antimony enhances the figure of merit significantly. $Ti_{0.5}Zr_{0.25}Hf_{0.25}NiSn$ produces a *ZT* in the range of 0.06 – 0.55 from 330 K – 900 K. However, *ZT* ranges from 0.23 – 0.82 for $Ti_{0.5}Zr_{0.25}Hf_{0.25}NiSn_{0.99}Sb_{0.01}$. Hence,

ZT_{max} was increased by a factor of 1.5 (Figure 39). This composition also displays the highest

average ZT among the doped samples. These results are a reflection of the comparatively high

PF and low κ values throughout the temperature range. The optimum properties for each dopant

concentration are provided in Table 8.

The ZT results obtained in this project for $Ti_{0.5}Zr_{0.25}Hf_{0.25}NiSn_{1-x}Sb_x$ do not match those

reported by N. Shutoh and S. Sakurada. Thus, a ZT of 1.5 was not obtained for the n-type

samples. The main reason for the discrepancy is due to differences in the Seebeck coefficients.

Those claimed by N. Shutoh and S. Sakurada are significantly higher than those measured in this

project.

Figure 39: $Ti_{0.5}Zr_{0.25}Hf_{0.25}NiSn_{1-x}Sb_x$ Figure of Merit

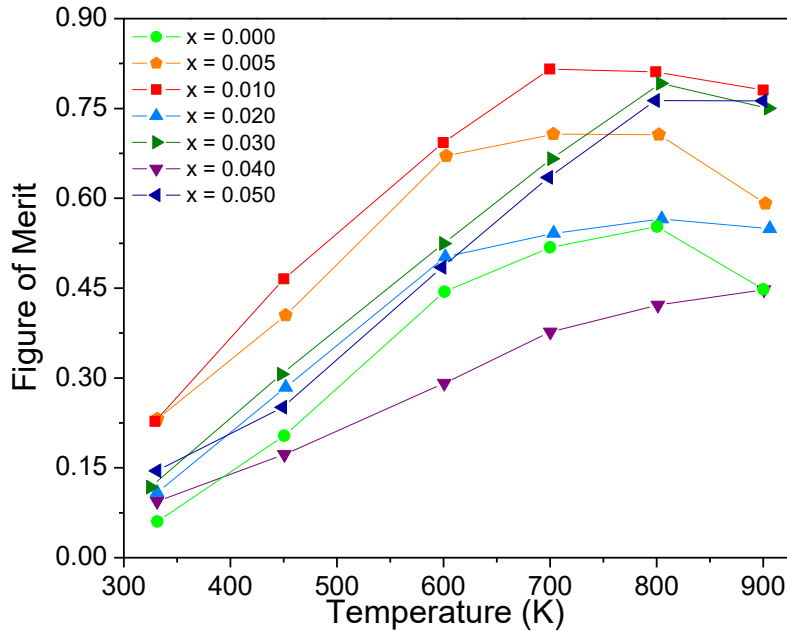Table 8: $Ti_{0.5}Zr_{0.25}Hf_{0.25}NiSn_{1-x}Sb_x$ Physical Properties at ZT_{max}

Sample	σ ($\Omega^{-1}cm^{-1}$)	S (μVK^{-1})	κ (W m^{-1}K^{-1})	T (K)	ZT_{max}
$Ti_{0.5}Zr_{0.25}Hf_{0.25}NiSn$	551	-188	2.81	800	0.55
$Ti_{0.5}Zr_{0.25}Hf_{0.25}NiSn_{0.995}Sb_{0.005}$	629	-206	2.65	700	0.71
$Ti_{0.5}Zr_{0.25}Hf_{0.25}NiSn_{0.99}Sb_{0.01}$	956	-186	2.84	700	0.82
$Ti_{0.5}Zr_{0.25}Hf_{0.25}NiSn_{0.98}Sb_{0.02}$	1083	-140	3.04	800	0.57
$Ti_{0.5}Zr_{0.25}Hf_{0.25}NiSn_{0.97}Sb_{0.03}$	1551	-147	3.42	800	0.79
$Ti_{0.5}Zr_{0.25}Hf_{0.25}NiSn_{0.96}Sb_{0.04}$	1309	-118	3.67	900	0.45
$Ti_{0.5}Zr_{0.25}Hf_{0.25}NiSn_{0.95}Sb_{0.05}$	2032	-140	4.16	800	0.76

4.3.4 ZrO$_2$ Nano-Composite Properties

Based on the results discussed in section 4.3.3, ZrO$_2$ nano-particles were added to $Ti_{0.5}Zr_{0.25}Hf_{0.25}NiSn_{0.99}Sb_{0.01}$ samples in an attempt to further improve the figure of merit. The nano-inclusions used for this project have a particle size of 100 nm and a density of 5.89 gcm^{-3}. $Ti_{0.5}Zr_{0.25}Hf_{0.25}NiSn_{0.99}Sb_{0.01}$ + y vol % ZrO$_2$ samples were hot-pressed for 2 hours at 1273 K. The densities of these samples are displayed below in Table 9.

Table 9: $Ti_{0.5}Zr_{025}Hf_{0.25}NiSn_{0.99}Sb_{0.01}$ + y vol % ZrO$_2$ Densities

ZrO$_2$ added	Experimental Density (gcm^{-3})	Theoretical Density (gcm^{-3})	Percent Density (%)
3 vol %	7.09	8.08	88
6 vol %	6.98	8.01	86
9 vol %	7.12	7.94	90

All samples showed decreasing electrical transport properties with increasing temperature from 330 K – 800 K, and a slightly increase in σ when heated to 900 K. Increasing the concentration of ZrO_2 nano-inclusions resulted in a decrease in σ (Figure 40a). There are two reasons as to why this trend occurs. Firstly, ZrO_2 is an insulator and thus has a lower electrical conductivity. Secondly, the number of interfaces increases as more ZrO_2 is added. Electrical conductivity for $Ti_{0.5}Zr_{0.25}Hf_{0.25}NiSn_{0.99}Sb_{0.01}$ + y vol % ZrO_2 ranges from $723 - 1248 \, \Omega^{-1}cm^{-1}$, $562 - 922 \, \Omega^{-1}cm^{-1}$ and $587 - 931 \, \Omega^{-1}cm^{-1}$ at 330 K, 800 K and 900 K respectively.
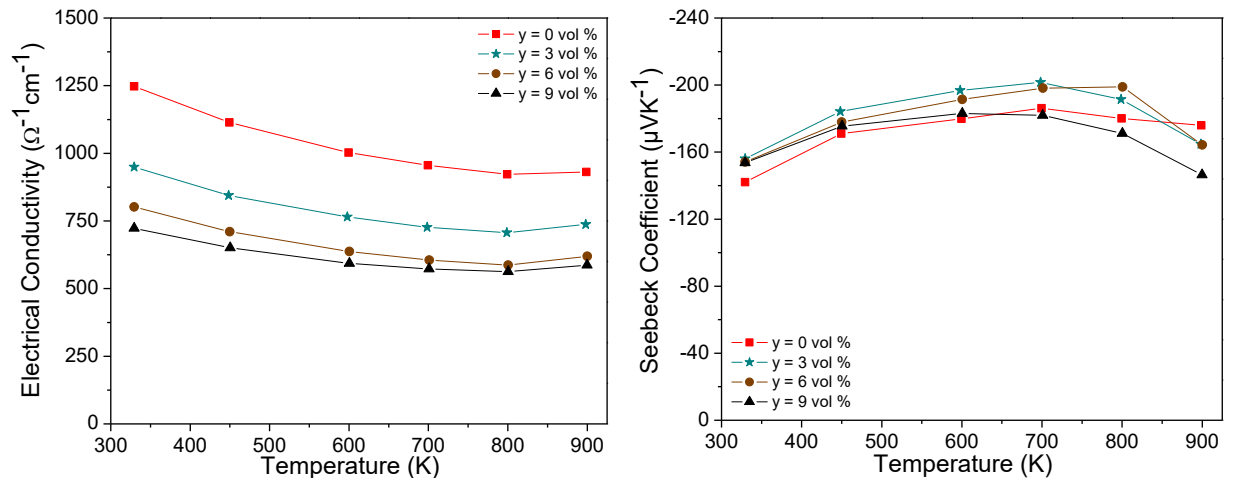
Figure 40: $Ti_{0.5}Zr_{0.25}Hf_{0.25}NiSn_{0.99}Sb_{0.01}$ + y vol % ZrO_2 (a) Electrical Conductivity (b) Seebeck Coefficient

Since electrical conductivity is inversely related to the Seebeck coefficient (Equation (8)), a slight increase in S was observed in the samples containing ZrO_2. At 330 K, $S = -142 \, \mu VK^{-1}$ for y = 0, and increases to $-155 \, \mu VK^{-1}$ when ZrO_2 is added. $Ti_{0.5}Zr_{0.25}Hf_{0.25}NiSn_{0.99}Sb_{0.01}$ + y vol % ZrO_2 samples produce a S_{max} around 700 K. The curve in Figure 40b shows a different S_{max} temperatures for y = 6 and y = 9. However, the S values obtained at these temperatures are within error from those obtained at 700 K. The Seebeck coefficient at 700 K is $-186 \, \mu VK^{-1}$, -202

μVK^{-1}, - 198 μVK^{-1}, and -182 μVK^{-1} for y = 0, 3, 6, and 9 respectively. Due to the bipolar effect, S decreases with temperature after 700 K.

The power factor of $Ti_{0.5}Zr_{0.25}Hf_{0.25}NiSn_{0.99}Sb_{0.01}$ + y vol % ZrO_2 decreases with increasing ZrO_2 content (Figure 41a). Therefore, the decrease in σ with increasing ZrO_2 content is more significant than the increase in S. At 300 K, PF ranges from 17 – 25 $\mu W\ cm^{-1}K^{-2}$. At low temperatures, $Ti_{0.5}Zr_{0.25}Hf_{0.25}NiSn_{0.99}Sb_{0.01}$ + y vol % ZrO_2 shows increasing PF with temperature. These samples exert maximum power output around 600 K. The obtained PF values at 600 K for y = 0, 3, 6 and 9 in order are 32 $\mu W\ cm^{-1}K^{-2}$, 30 $\mu W\ cm^{-1}K^{-2}$, 23 $\mu W\ cm^{-1}K^{-2}$, and 20 $\mu W\ cm^{-1}K^{-2}$. PF decreases with temperature from 600 – 900 K. At 900 K, PF ranges from 13 – 29 $\mu W\ cm^{-1}K^{-2}$.
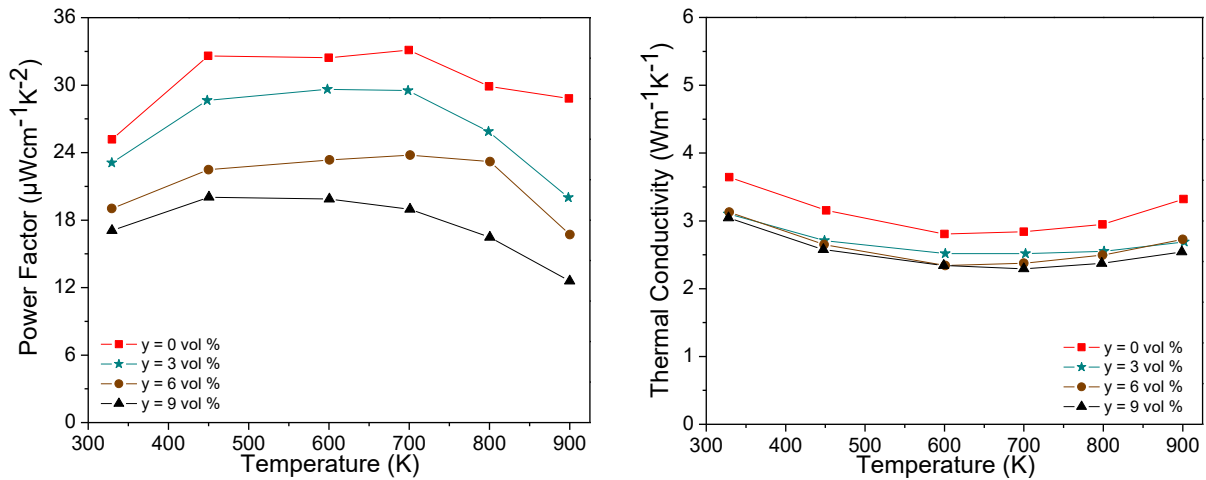
Figure 41: $Ti_{0.5}Zr_{0.25}Hf_{0.25}NiSn_{0.99}Sb_{0.01}$ + y vol % ZrO_2 (a) Power Factor (b) Total Thermal Conductivity

To restate, nano-materials are used in TE research to decrease total thermal conductivity by lowering the lattice contribution. Reductions in κ, κ_l and κ_e were observed by incorporating

ZrO$_2$ nano-materials in the structure. Bulk ZrO$_2$ produces similar thermal conductivity values when compared to these HH materials. At room temperature, $\kappa \approx 3.3$ W m^{-1}K^{-1} for bulk ZrO$_2$. All nano-composite samples produced κ values within error at 330 K. By adding ZrO$_2$ to Ti$_{0.5}$Zr$_{0.25}$Hf$_{0.25}$NiSn$_{0.99}$Sb$_{0.01}$, κ decreased from 3.64 W m^{-1}K^{-1} to 3.09 W m^{-1}K^{-1} at 330 K. At low temperatures, κ decreases with increasing temperature due to significant decreases in κ_l. Ti$_{0.5}$Zr$_{0.25}$Hf$_{0.25}$NiSn$_{0.99}$Sb$_{0.01}$ + y vol % ZrO$_2$ materials show minimum κ values around 600 K. At this temperature, $\kappa = 2.81$ Wm^{-1}K^{-1} for y = 0, 2.52 W m^{-1}K^{-1} for y = 3, and 2.34 W m^{-1}K^{-1} for y > 3. Above this temperature, increases in κ_e become more significant and result in higher κ with increasing temperature. At 900 K, $\kappa = 3.32$ W m^{-1}K^{-1} without ZrO$_2$ and approximately 2.65 W m^{-1}K^{-1} with nano-particles.

The electronic contribution to thermal conductivity decreases with increasing ZrO$_2$ concentration (Figure 42a). This is a product of decreasing electrical conductivity, which is lowered when the number of interfaces increases. From 330 – 900 K, κ_e increases with temperature. At 330 K and 900 K, κ_e ranges from 0.41 – 0.72 W m^{-1}K^{-1} and 0.92 – 1.39 W m^{-1}K^{-1} correspondingly.

By adding ZrO$_2$ nano-additions to Ti$_{0.5}$Zr$_{0.25}$Hf$_{0.25}$NiSn$_{0.99}$Sb$_{0.01}$, the lattice contribution to thermal conductivity decreases (Figure 42b). When below 700 K, κ_l values for the ZrO$_2$ containing samples fall within error. By introducing these materials to the matrix, κ_l decreased from 2.93 Wm^{-1}K^{-1} to 2.63 Wm^{-1}K^{-1} at 330 K and 1.74 Wm^{-1}K^{-1} to 1.67 Wm^{-1}K^{-1} at 600 K. In order, the calculated κ_l values are 1.93 Wm^{-1}K^{-1}, 1.57 Wm^{-1}K^{-1}, 1.78 Wm^{-1}K^{-1}, and 1.63 Wm^{-1}K^{-1} for y = 0, 3, 6, and 9.
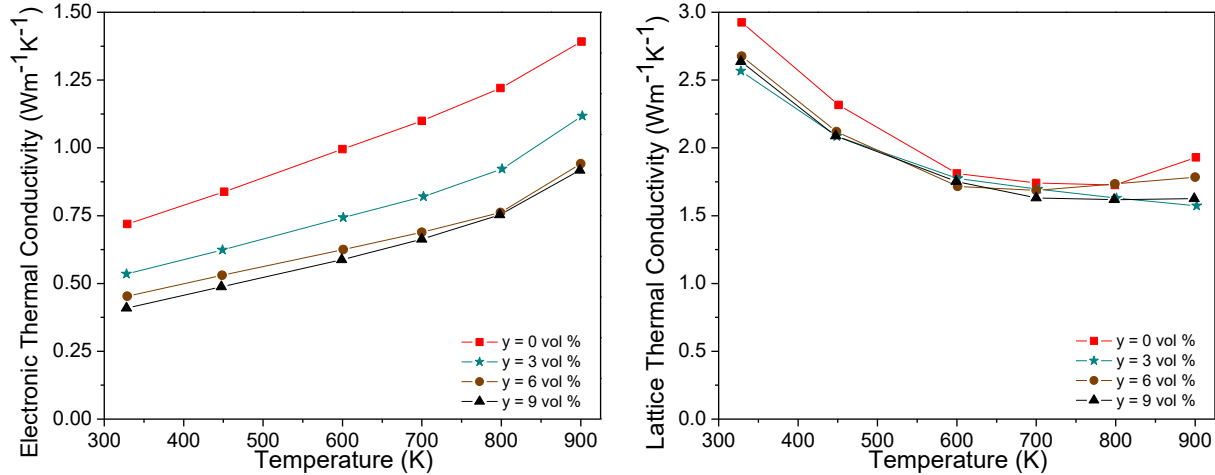
Figure 42: $Ti_{0.5}Zr_{0.25}Hf_{0.25}Ni\ Sn_{0.99}Sb_{0.01}$ + y vol % ZrO_2 (a) Electronic Contribution to Thermal Conductivity (b) Lattice Contribution to Thermal Conductivity

The figure of merit from 330 K – 900 K is shown in Figure 43 for $Ti_{0.5}Zr_{0.25}Hf_{0.25}NiSn_{0.99}Sb_{0.01}$ with and without ZrO_2 nano-materials. For y ≥ 6, the observed reductions in κ_l were less significant than those in the *PF*. Therefore, these samples produced lower figures of merit than $Ti_{0.5}Zr_{0.25}Hf_{0.25}NiSn_{0.99}Sb_{0.01}$. A higher *ZT* was obtained for y = 3 from 330 – 800 K. However, the values obtained fall within error to those received without nano-inclusions. Therefore, *ZT* was not improved by incorporating nano-particles in the structure. The insignificant decrease in κ_l is likely due to ZrO_2 large particle sizes. This could mean that the particle sizes were too large to begin with, or that agglomeration occurred and increased the apparent size of the nano-particles. Further SEM-EDX experiments are required to determine the answer to these two possibilities. At 330 K, *ZT* ranges from 0.18 – 0.24. Based on the *ZT* curves, $Ti_{0.5}Zr_{0.25}Hf_{0.25}NiSn_{0.99}Sb_{0.01}$ + y vol % ZrO_2 produces a maximum figure of merit between 600 and 700 K. The best thermoelectric properties of these samples are displayed in table 10.
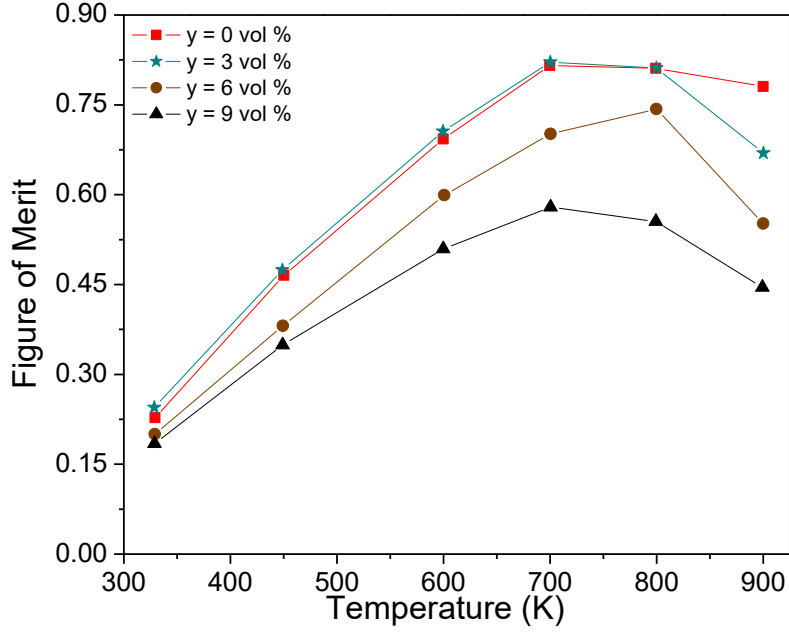
Figure 43: $Ti_{0.5}Zr_{0.25}Hf_{0.25}NiSn_{0.99}Sb_{0.01}$ + y vol % ZrO_2 Figure of Merit

Table 10: $Ti_{0.5}Zr_{0.25}Hf_{0.25}NiSn_{0.99}Sb_{0.01}$ + y vol % ZrO_2 Physical Properties at ZT_{max}

Sample	σ $(\Omega^{-1}cm^{-1})$	S (μVK^{-1})	κ $(W\ m^{-1}K^{-1})$	T (K)	ZT_{max}
$Ti_{0.5}Zr_{0.25}Hf_{0.25}NiSn_{0.99}Sb_{0.01}$	956	-186	2.84	700	0.82
$Ti_{0.5}Zr_{0.25}Hf_{0.25}NiSn_{0.99}Sb_{0.01}$ + 3 vol % ZrO_2	726	-202	2.52	700	0.82
$Ti_{0.5}Zr_{0.25}Hf_{0.25}NiSn_{0.99}Sb_{0.01}$ + 6 vol % ZrO_2	587	-199	2.50	800	0.74
$Ti_{0.5}Zr_{0.25}Hf_{0.25}NiSn_{0.99}Sb_{0.01}$ + 9 vol % ZrO_2	573	-182	2.29	700	0.58

5.0 Conclusions

A variety of undoped and doped MNiSn (M = Ti, Zr, Hf) materials were successfully synthesized. PXRD diagrams and EDX spectroscopy results indicate high purity samples.

In this project, simple ternaries like TiNiSn and HfNiSn displayed maximum figures of merit of 0.33 and 0.28 respectively. These properties were significantly improved by alloying the M site with Ti, Zr, and Hf. A $ZT_{max} = 0.55$ at 800 K was obtained for $Ti_{0.5}Zr_{0.25}Hf_{0.25}NiSn$; more than a factor of 1.5 times greater than the ternaries.

Physical property measurements were conducted on $Ti_{0.5}Zr_{0.25}Hf_{0.25}Co_xNi_{1-x}Sn$ samples with Co concentrations ranging from $0.01 \leq x \leq 0.20$. A transition from n-type to p-type conduction was observed at x = 0.04. In this project, the best p-type properties were observed in $Ti_{0.5}Zr_{0.25}Hf_{0.25}Co_{0.15}Ni_{0.85}Sn$. A $ZT_{max} = 0.18$ at 800 K was measured for this material. This value is drastically less than the $ZT_{max} = 0.8$ measured by X. Yan et al. for ball-milled $Zr_{0.5}Hf_{0.5}CoSb_{0.8}Sn_{0.2}$; the best p-type Half Heusler material to date.[20]

Doping $Ti_{0.5}Zr_{0.25}Hf_{0.25}NiSn$ with small amounts of antimony leads to considerable enhancements in the figure of merit. $Ti_{0.5}Zr_{0.25}Hf_{0.25}NiSn_{1-x}Sb_x$ materials were synthesized and measured with dopant concentrations varying from $0.005 \leq x \leq 0.05$. Measurements taken in this project imply that $Ti_{0.5}Zr_{0.25}Hf_{0.25}NiSn_{0.99}Sb_{0.01}$ produces the best thermoelectric properties. From 330 – 900 K, this material produces the highest average ZT, with a measured $ZT_{max} = 0.82$ at 700 K. These results do not match those reported by N. Shutoh and S. Sakurada. They reported that $Ti_{0.5}Zr_{0.25}Hf_{0.25}NiSn_{0.99}Sb_{0.002}$ produces the best properties with a ZT_{max} of 1.5 at 700 K.[19] The

main reason for the discrepancy is due to dissimilarities in Seebeck coefficients. Those claimed by N. Shutoh and S. Sakurada are substantially higher than those measured in this project.

ZrO_2 nano-inclusions varying from 3 – 9 vol % were added to $Ti_{0.5}Zr_{0.25}Hf_{0.25}NiSn_{0.99}Sb_{0.01}$ in an attempt to improve the figure of merit. Although improvements were observed in thermal conductivity, power factor losses resulted in no enhancements towards the figure of merit.

To reiterate, $Ti_{0.5}Zr_{0.25}Hf_{0.25}NiSn_{0.99}Sb_{0.01}$ is an effective material for converting heat into electricity. With more research, these compounds can be further optimized and potentially become the most efficient *n*-type Half Heusler material. By reducing the average grain size through ball-milling, *ZT* could be improved from a reduction in thermal conductivity.[51] This could also lead to higher sample densities after hot-pressing. Densities could also be improved by pressing samples via spark plasma sintering. Although no improvements were observed in this project by adding ZrO_2, higher *ZT* may be observed with smaller concentrations and/or smaller particle sizes. The *M* site of these materials has been optimized by alloying. However, no work has been carried out on the nickel and tin sites of the material. Alloying these sites may also improve physical properties by reducing thermal conductivity. This could be carried out with palladium and germanium. Research has already shown that alloying $Zr_{0.5}Hf_{0.5}NiSn$ with Pd and alloying Mg_2Si with Ge improves the dimensionless figure of merit.[18, 39 62-63] Figure 44 summarizes all the work that has been completed in this project.
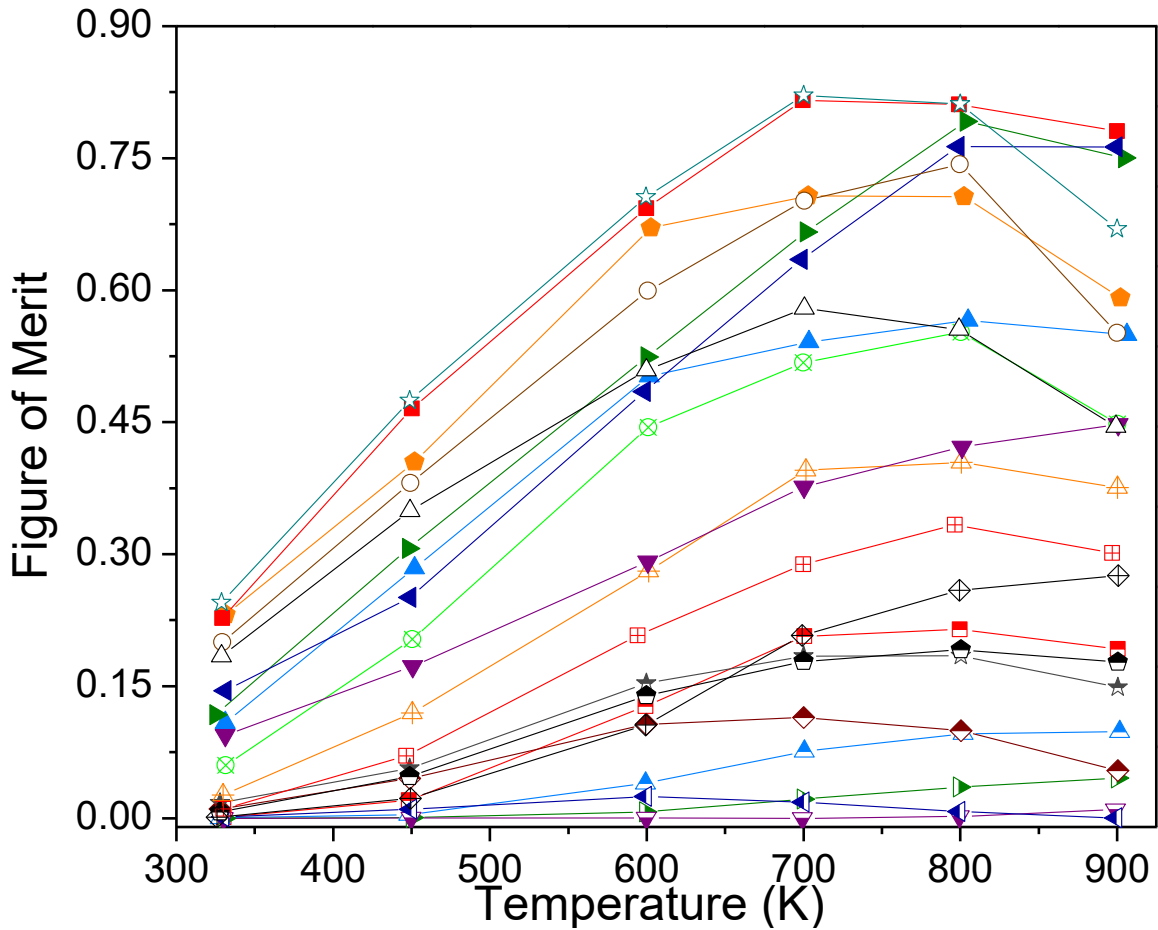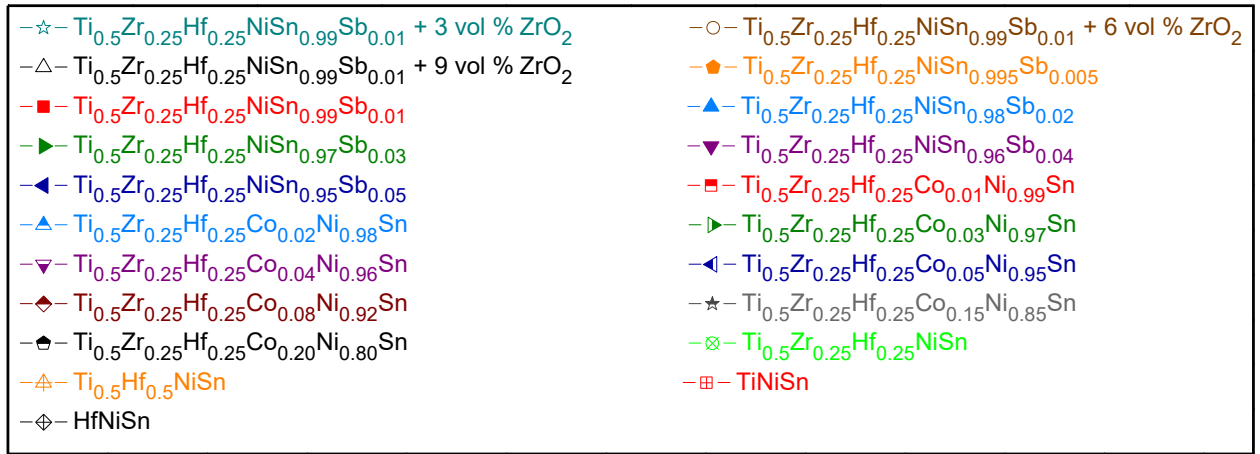
Figure 44: The Figure of Merit for all Undoped and Doped *M*NiSn Half-Heusler Materials

Synthesized in this Project

References

1. Kleinke, H. *Chemistry of Materials* **2010**, *22*, 604-611.

2. Saidur, R.; Rezaei, M.; Muzammil, W.; Hassan, M.; Paria, S.; Hasanuzzaman, M. *Renewable and Sustainable Energy Reviews* **2012**, *16*, 5649-5659.

3. Yang, J.; Stabler, F. R. *Journal of Electronic Materials* **2009**, *38*, 1245-1251.

4. Gelbstein, Y.; Tal, N.; Yarmek, A.; Rosenberg, Y.; Dariel, M. P.; Ouardi, S.; Balke, B.; Felser, C.; Köhne, M. *Journal of Materials Research* **2011**, *26*, 1919.

5. Bux, S. K.; Yeung, M. T.; Toberer, E. S.; Snyder, G. J.; Kaner, R. B.; Fleurial, J.-P. *Journal of Materials Chemistry* **2011**, *21*, 12259-12266.

6. Fiameni, S.; Battiston, S.; Boldrini, S.; Famengo, A.; Agresti, F.; Barison, S.; Fabrizio, M. *Journal of Solid State Chemistry* **2012**, *193*, 142-146.

7. Minnich, A.; Dresselhaus, M.; Ren, Z.; Chen, G. *Energy & Environmental Science* **2009**, *2*, 466-479.

8. Jeung, S-K., *Optimization of Type-I Clathrates for Thermoelectric Properties* **2012**. University of Waterloo, Ontario.

9. Zhu, Y., *Early/Late Transition Metal Antimonides: Preparation of Thermoelectric Materials* **2002**. University of Waterloo, Ontario.

10. DiSalvo, F. J. *Science* **1999**, *285*, 703-706.

11. Chen, G.; Dresselhaus, M.; Dresselhaus, G.; Fleurial, J.-P.; Caillat, T. *International Materials Reviews* **2003**, *48*, 45-66.

12. Szczech, J. R.; Higgins, J. M.; Jin, S. *Journal of Materials Chemistry* **2011**, *21*, 4037-4055.

13. Franz, M. *Nature Materials* **2010**, *9*, 536-537.

14. Tritt, T. *Recent Trends in Thermoelectric Materials Research, Part Two*; Academic Press **2000**; Vol. 70.

15. Alijani, V.; Winterlik, J.; Fecher, G. H.; Naghavi, S. S.; Chadov, S.; Gruhn, T.; Felser, C. *Journal of Physics: Condensed Matter* **2012**, *24*, 046001.

16. Casper, F.; Graf, T.; Chadov, S.; Balke, B.; Felser, C. *Semiconductor Science and Technology* **2012**, *27*, 063001.

17. Bhattacharya, S.; Pope, A.; Littleton IV, R.; Tritt, T. M.; Ponnambalam, V.; Xia, Y.; Poon, S. *Applied Physics Letters* **2000**, *77*, 2476-2478.

18. Chen, L.; Huang, X.; Zhou, M.; Shi, X.; Zhang, W. *Journal of Applied Physics* **2006**, *99*, 064305.

19. Shutoh, N.; Sakurada, S. *Journal of Alloys and Compounds* **2005**, *389*, 204-208.

20. Yan, X.; Joshi, G.; Liu, W.; Lan, Y.; Wang, H.; Lee, S.; Simonson, J.; Poon, S.; Tritt, T.; Chen, G. *Nano Letters* **2010**, *11*, 556-560.

21. Kleinke, H. *Inorganic Chemistry* **2001**, *40*, 95-100.

22. Katayama, T.; Kim, S. W.; Kimura, Y.; Mishima, Y. *Journal of Electronic Materials* **2003**, *32*, 1160-1165.

23. Qiu, P.; Huang, X.; Chen, X.; Chen, L. *Journal of Applied Physics* **2009**, *106*, 103703.

24. Wu, T.; Jiang, W.; Li, X.; Zhou, Y.; Chen, L. *Journal of Applied Physics* **2007**, *102*, 103705.

25. Kawano, K.; Kurosaki, K.; Sekimoto, T.; Muta, H.; Yamanaka, S. *Applied Physics Letters* **2007**, *91*, 062115.

26. Oxley, D.; Tebble, R.; Williams, K. *Journal of Applied Physics* **1963**, *34*, 1362-1364.

27. Oxley, D.; Tebble, R.; Slack, C.; Williams, K. *Nature* **1962**, *197*, 465.

28. Kanomata, T.; Kikuchi, M.; Yamauchi, H. *Journal of alloys and compounds* **2006**, *414*, 1-7.

29. Müller, R. A.; Desilets-Benoit, A.; Gauthier, N.; Lapointe, L.; Bianchi, A.; Maris, T.; Zahn, R.; Beyer, R.; Green, E.; Wosnitza, J. *Physical Review B* **2015**, *92*, 184432.

30. Pavlosiuk, O.; Kaczorowski, D.; Fabreges, X.; Gukasov, A.; Wiśniewski, P. *Scientific Reports* **2016** *6,* 18797.

31. Hames, F. *Journal of Applied Physics* **1960**, *31*, 370.

32. Laughlin, D.; Willard, M.; McHenry, M. *Phase Transformations and Evolution in Materials* **2000**, 121-137.

33. X. Shi, J. Yang, S. Bai, J. Yang, H. Wang, M. Chi, J. R. Salvador, W. Zhang, L. Chen, and W. Wong-Ng. *Adv. Funct. Mater* **2010**, *20*, 755.

34. Oudah, M., *Optimization of Thermoelectric Chalcogenides* **2014**. University of Waterloo, Ontario.

35. Shams, R.,*Thermoelectric Properties of Materials Based on Double Filled Type-I Clathrates* **2015**. University of Waterloo, Ontario.

36. Soheilnia, N., *Thermoelectric Properties of New Transition Metal Arsenides and Antimonides* **2007**. University of Waterloo, Ontario.

37. Guo, Q., *Thallium Tellurides as Thermoelectrics* **2015**. University of Waterloo, Ontario.

38. Truong, D. Y. N., *Thermoelectric Properties of Higher Manganese Silicides* **2015**. University of Waterloo, Ontario.

39. Farahi, N. *Magnesium Silicide Based Thermoelectric Nanocomposites* **2016**. University of Waterloo, Ontario.

40. Rowe, D. M. *CRC Handbook of Thermoelectrics*; CRC press **1995**, 212-222.

41. Goldsmid, H. J. *Introduction to Thermoelectricity*; Springer Science & Business Media **2009**, *121*, 4.

42. Graf, T.; Felser, C.; Parkin, S. S. *Progress in Solid State Chemistry* **2011**, *39*, 1-50.

43. Hermet, P.; Niedziolka, K.; Jund, P. *RSC Advances* **2013**, *3*, 22176-22184.

44. Kreiner, G.; Kalache, A.; Hausdorf, S.; Alijani, V.; Qian, J. F.; Shan, G.; Burkhardt, U.; Ouardi, S.; Felser, C. *New Mn$_2$-based Heusler Compounds* **2014**, *640*, 738-752.

45. Luo, H.; Meng, F.; Liu, G.; Liu, H.; Jia, P.; Liu, E.; Wang, W.; Wu, G. *Intermetallics* **2013**, *38*, 139-143.

46. Yabuuchi, S.; Okamoto, M.; Nishide, A.; Kurosaki, Y.; Hayakawa, J. *Applied Physics Express* **2013**, *6*, 025504.

47. Nishino, Y.; Deguchi, S.; Mizutani, U. *Physical Review B* **2006**, *74*, 115115.

48. Mikami, M.; Kinemuchi, Y.; Ozaki, K.; Terazawa, Y.; Takeuchi, T. *Journal of Applied Physics* **2012**, *111*, 093710.

49. Shen, Q.; Chen, L.; Goto, T.; Hirai, T.; Yang, J.; Meisner, G.; Uher, C. *Applied Physics Letters* **2001**, *79*, 4165-4167.

50. Katsuyama, S.; Matsuo, R.; Ito, M. *Journal of Alloys and Compounds* **2007**, *428*, 262-267.

51. Zou, M.; Li, J.-F.; Du, B.; Liu, D.; Kita, T. *Journal of Solid State Chemistry* **2009**, *182*, 3138-3142.

52. Xie, W.; Jin, Q.; Tang, X. *Journal of Applied Physics* **2008**, *103*, 43711-43711.

53. Schwall, M.; Balke, B. *Physical Chemistry Chemical Physics* **2013**, *15*, 1868-1872.

54. Culp, S. R.; Simonson, J.; Poon, S. J.; Ponnambalam, V.; Edwards, J.; Tritt, T. M. *Applied Physics Letters* **2008**, *93*, 2105.

55. Sekimoto, T.; Kurosaki, K.; Muta, H.; Yamanaka, S. *Journal of Alloys and Compounds* **2006**, *407*, 326-329.

56. Wu, T.; Jiang, W.; Li, X.; Bai, S.; Liufu, S.; Chen, L. *Journal of Alloys and Compounds* **2009**, *467*, 590-594.

57. Takas, N. J.; Sahoo, P.; Misra, D.; Zhao, H.; Henderson, N. L.; Stokes, K.; Poudeu, P. F. *Journal of Electronic Materials* **2011**, *40*, 662-669.

58. Downie, R. A.; MacLaren, D.; Bos, J.-W. *Journal of Materials Chemistry A* **2014**, *2*, 6107-6114.

59. Downie, R. A; MacLaren, D.; Smith, R.; Bos, J.-W. *Chemical Communications* **2013**, *49*, 4184-4186.

60. Stadnyk, Y.; Horyn, A.; Romaka, V.; Gorelenko, Y.; Romaka, L.; Hlil, E.; Fruchart, D. *Journal of Solid State Chemistry* **2010**, *183*, 3023-3028.

61. Jeitschko, W. *Metallurgical Transactions* **1970**, *1*, 3159-3162.

62. Akasaka, M.; Iida, T.; Nishio, K.; Takanashi, Y. *Thin Solid Films* **2007**, *515*, 8237-8241.

63. Farahi, N.; Prabhudev, S.; Botton, G. A.; Zhao, J.; John, S. T.; Liu, Z.; Salvador, J. R.; Kleinke, H. *Journal of Alloys and Compounds* **2015**, *644*, 249-255.

64. Farahi, N.; VanZant, M.; Zhao, J.; John, S. T.; Prabhudev, S.; Botton, G. A.; Salvador, J. R.; Borondics, F.; Liu, Z.; Kleinke, H. *Dalton Transactions* **2014**, *43*, 14983-14991.